

On the impact of the supernova subsamples in reducing the Hubble tension

Gonçalo Martins¹, Santiago González-Gaitán^{2,3}, João Duarte¹ and Ana M. Mourão¹

¹ CENTRA, Instituto Superior Técnico, Universidade de Lisboa, Av. Rovisco Pais 1, 1049-001 Lisboa, Portugal
e-mail: goncalo.jose.lourenco.martins@tecnico.ulisboa.pt

² Instituto de Astrofísica e Ciências do Espaço, Faculdade de Ciências, Universidade de Lisboa, Ed. C8, Campo Grande, 1749-016 Lisbon, Portugal

³ European Southern Observatory, Alonso de Córdova 3107, Casilla 19, Santiago, Chile

ABSTRACT

The persistent $4\text{--}6\sigma$ discrepancy between early- and late-time measurements of the Hubble constant (H_0) is known as the "Hubble tension" and represents one of the major open problems in modern cosmology. In this work, we investigate how differences in light-curve parameters such as colour (c) and stretch (x_1), and host galaxy properties such as the host stellar mass (M) and specific star formation rate (sSFR) between the calibration and Hubble Flow (HF) Type Ia supernovae (SNe Ia) samples used by SH0ES affect the SN luminosity standardization and the H_0 estimation. To do that, we generate subsamples from both samples and use them to estimate H_0 , M_B , α , β , Δ_{host} and σ_{int} . Both one- and multi-dimensional Kolmogorov–Smirnov tests are used to evaluate the consistency between the subsamples property distributions and analyze how the estimated parameters vary with the better matching of the subsamples. We find that the calibration sample is not fully representative of the HF sample, particularly in the host's M and sSFR. Improving consistency between subsamples leads to changes in H_0 , M_B , α and σ_{int} as the samples become more consistent, although overall values remain broadly stable. More consistent subsamples also tend to produce a mass step consistent with zero within 1σ . When disentangling SN subpopulations using different approaches, we identify persistent differences in H_0 ($\sim 2\text{--}3\sigma$) and M_B ($\sim 2\sigma$) between low- and high-stretch SN Ia subpopulations: we find $H_0 = 75.27 \pm 1.18 \text{ km s}^{-1} \text{ Mpc}^{-1}$ for low-stretch and $H_0 = 71.25 \pm 1.59 \text{ km s}^{-1} \text{ Mpc}^{-1}$ for high-stretch, resulting in a Hubble tension of 6.07σ and 2.52σ , respectively. These differences highlight how multiple SNIa sub-populations likely present variations in dust properties and intrinsic colour that are not captured by the standard single β parameterization and that affect cosmology. By considering these two SN subpopulations when estimating a single Hubble parameter for all SNe, we obtain $H_0 = 73.78 \pm 2.17 \text{ km s}^{-1} \text{ Mpc}^{-1}$, a much larger uncertainty than normally quoted and resulting in decreasing the tension with the Planck measurement from 5.87σ to about 2.86σ . Moreover, our results also suggest that the mass step may arise from an over-correction of more than one SN subpopulation associated to different environments.

Key words. Cosmology: distance scale – Cosmology: cosmological parameters – Stars: supernovae

1. Introduction

According to the Friedmann-Lemaître equations, the expansion of the Universe is redshift-dependent and can be characterized by the Hubble parameter $H(z)$. The Hubble constant (H_0) corresponds to the present time ($z=0$) value of this parameter, giving us the Universe's local expansion rate and providing crucial information about its age and history (Freedman & Madore 2010).

Given the importance of this parameter to understand our Universe, two main pathways of calculating the value of H_0 were developed and improved over the years. The first approach relies on early universe measurements such as the Cosmic Microwave Background (CMB), which assumes a flat Λ CDM (Lambda Cold Dark Matter) cosmological model (Peebles 1984), to infer local values of expansion, i.e. $H_0 = 67.4 \pm 0.5 \text{ km s}^{-1} \text{ Mpc}^{-1}$ (Planck Collaboration et al. 2020). The second approach relies on later measurements from the local universe based on the cosmic distance ladder involving typically observations of SNe Ia and closer luminous objects such as Cepheids to calibrate their distances, favoring higher values of $H_0 = 73.04 \pm 1.04 \text{ km s}^{-1} \text{ Mpc}^{-1}$ (Riess et al. 2022).

Analyzing the different estimations of H_0 from the early and late-time measurements it is possible to identify a consistent statistically significant tension that varies from 4 to 6σ disagree-

ment between both predictions, with higher values of H_0 obtained locally. This discrepancy is known as the "Hubble tension" and is considered one of the major open problems in modern cosmology. This difference can indicate the need for new physics (e.g., Hu & Wang 2023) or, at the very least, unexpectedly large systematic errors in either or both of the two principal measurements.

The cosmic distance ladder is a technique used to determine cosmological distances in the nearby universe, starting by using geometric distance measurements, such as parallax, to calibrate nearby standard candles located in our galaxy such as Cepheid variables. These are luminous variable stars of different brightnesses but with a well-defined Period-Luminosity relation (Leavitt 1908). Modern calibrations have refined this relation to include metallicity effects, leading to the Period-Luminosity-Metallicity (PLZ; Groenewegen 2018). Once calibrated, this relation can be used to obtain the distances to Cepheids located in nearby galaxies, which can not be precisely computed through parallax. These nearby galaxies can also contain type Ia Supernovae (SNe Ia), which are very bright explosions of carbon-oxygen white dwarfs in binary systems (Hoyle & Fowler 1960) allowing us to detect them in even more distant galaxies. Even though SNe Ia do not have a known universal peak magnitude,

they serve as standardizable candles whose observed light curves can be used to obtain their distances. The observation of nearby events of this type showed that all explosions had quite similar peak luminosities and light curves with relatively small variations (Branch & Tammann 1992) that can be standardized by applying some empirical corrections based on the light curve shape-luminosity (Phillips 1993) and colour-luminosity relations expressed in the two-parameter correction model proposed by Tripp (1998). However, as observed by Sullivan et al. (2010) and Kelly et al. (2010), after the application of these two corrections, SNe Ia detected in higher-mass galaxies appear consistently over-luminous, such that a significant mass step is evident in the difference between their corrected and predicted luminosities. The nature of this third correction is still not fully understood.

It is important to make a clear distinction between the two samples of SNe Ia involved in the distance ladder. On the one hand, we have the calibration sample, which includes SNe Ia located in nearby galaxies that also host Cepheid variables. This sample allows us to break the well-known degeneracy between the estimated absolute peak magnitude of SNe in the B-band (M_B) and H_0 (e.g., Camarena & Marra 2021). On the other hand, we have the Hubble Flow (HF) sample, which consists of SNe Ia in more distant galaxies. Together with the calibration sample, this sample enables us to estimate all the correction parameters used in the SNe Ia luminosities standardization, as well as the M_B and H_0 parameters (Riess et al. 2016).

Although the current study will only focus on the traditional Cepheid-based distance ladder, several alternative methods have been adopting Brightness Fluctuations (SBF; Khetan et al. 2021), J-region Asymptotic Giant Branch (JAGB; Huang et al. 2020), and the Tip of the Red Giant Branch (TRGB; Freedman et al. 2019) stars as complementary or substitute nearby distance indicators to Cepheids. Among all H_0 estimations relying on a local calibration, the TRGB-based approach, which results in a value of $H_0 = 69.8 \pm 1.7 \text{ km s}^{-1} \text{ Mpc}^{-1}$ (Freedman et al. 2019), is the one that exhibits the largest discrepancy (at the level of $\sim 1.7 \sigma$) compared to the Cepheid-based determination by Riess et al. (2022). Additional efforts have explored the use of Type II supernovae as alternative cosmological standard candles (De Jaeger et al. 2020; Vogl, C. et al. 2025), as well as entirely independent ladder methods such as standard sirens (Abbott et al. 2017) and gravitational lensing time-delay cosmography (Birrer et al. 2024).

A variety of potential systematic effects associated with the general framework of supernova analysis such as photometric calibrations, light curve fitting, Milky Way extinction, and the accuracy of redshifts, including peculiar velocity corrections have been demonstrated to have negligible influence on the determination of the Hubble constant, as shown by Brout et al. (2022) and Steinhardt et al. (2020). A detailed review of proposed solutions for the Hubble tension can be found in Valentino et al. (2021).

Cepheid variables are predominantly found in late-type, star-forming galaxies such as the Milky Way, and are normally observed in face-on galaxies to reduce the effects from enhanced crowding and reddening issues (e.g., Anderson 2024). To mitigate potential biases in dust extinction and reddening between the calibration sample SNe and those from the Hubble Flow hosted in passive environments (e.g., Rigault et al. 2015), Riess et al. (2022) selected similar late-type galaxies for the calibration and HF samples, assuming that the dust extinction laws are correlated with the star formation rate (SFR) and the stellar mass formed in each galaxy (e.g., Salim et al. 2018) and so that the

extinction law can be customized based on the galaxy type. Following this assumption, large, star-forming spiral hosts of SNe Ia have, presumably, a similar dust extinction law to the Milky Way, which helps maintain consistency across all rungs of the local distance ladder. However, this selection alone may not be sufficient to ensure that the dust properties are consistent between the samples. Moreover, the extinction model adopted in the simulations that are used for bias corrections in the SNe Ia luminosity standardization in studies such as the one by Brout et al. (2022) is trained on the unrestricted Hubble flow sample, which includes galaxies of all morphological types, and then extrapolated to the calibration galaxies (e.g., Popovic et al. 2023), potentially introducing a significant bias in the correction.

As shown in several studies such as Sullivan et al. (2010) and Pruzhinskaya et al. (2020), there is a dependency between the SNe light curve properties and their host environment and morphology. Studies by Nicolas et al. (2021) and more recently by Ginolin et al. (2025) suggest that the stretch-magnitude relation might be non-linear with a strong correlation with the SN environment and redshift, contrarily to the relation commonly adopted in cosmological analyses. This non-linearity may reflect the presence of distinct SN Ia populations, as revealed by the bimodal behavior identified in the stretch distribution of both studies. Specifically, a low-stretch mode is associated with SNe Ia in old stellar populations, typically hosted by redder and/or more massive galaxies, unlike the high-stretch mode that is shared by both young and old environments. These results are also in agreement with the findings by Rigault et al. (2020a), which confirms that the SN Ia light curve stretch distribution reflects an intrinsic SN property that depends on the progenitor age, with younger SNe Ia predominantly populating the higher stretch mode and constituting an intrinsically more homogeneous population. The work done by Wojtak & Hjorth (2022) also claims for a strong evidence that SN standardization within the calibration sample requires a significantly steeper colour correction slope compared to the Hubble Flow sample. This discrepancy points to an intrinsic tension between the calibration and HF samples and assumes the existence of overlapping SN Ia subpopulations, primarily distinguished by differences in their mean stretch parameter. According to Wojtak et al. (2023), SNe belonging to the high-stretch population tend to be intrinsically bluer and exhibit approximately twice the level of dust reddening along their lines of sight relative to those from the low-stretch population.

Other studies such as the one by Duarte et al. (2023) reinforce the idea that the mass step correction is partially driven by differences in supernova intrinsic and extrinsic properties, finding that this effect cannot be entirely explained as a dust systematic, as suggested by Brout & Scolnic (2021). There are also some works that report a relation between the galaxies ages and the mass step, as the one by Chung et al. (2023) and Wiseman et al. (2023a), and that the mass step can vary based on whether a supernova is located in the inner or outer region of the galaxy (Toy et al. 2025).

Considering all the results above, it is possible to conclude that the accuracy of the distance ladder method also relies on the precise matching of the supernovae population properties and their host environments both in the calibration and in the Hubble Flow galaxies, which is taken for granted in almost all studies that use this technique to estimate the H_0 values. However, we can have a calibration sample whose SNe Ia are not representative of the ones that we can find in the HF sample, both in terms of their intrinsic properties as in terms of their host galaxies properties, which can introduce a possible bias in the calibration.

In this study, we propose to investigate and compare the supernovae light curve parameters as well as their host galaxy properties of both the calibration and Hubble Flow samples, see if there are subsamples from the calibration and HF samples that better match each other, understand the impact that this sample matching has in the Hubble parameter estimation and derive a more accurate calibration for SNe Ia luminosities. The dataset used in this study and its treatment are detailed in Section 2. The methodology used to obtain the correction parameters, as well as the values of the SNe absolute magnitude in the B-band (M_B) and H_0 is presented in Section 3. The analysis and results can be found in Section 4. In Subsection 4.1, we compare both calibration and HF SNe samples property distributions, while in Subsection 4.2 we generate pairs of random subsamples from the calibration and Hubble flow samples. In Subsection 4.3 we see if there is any relation between the better matching of the generated subsamples property distributions and the estimated H_0 , M_B , α , β , Δ_{host} and σ_{int} . We further investigate the impact of accounting for the properties of the SNe within the generated subsamples in our analysis in Subsection 4.4, as well as the effect of using SNe from different property bins on the estimated H_0 , M_B , and the correction parameters in Subsection 4.5, as a way to assess the different SN subpopulations within the sample. In particular, we focus on stretch-based subpopulations and construct subsamples from distinct stretch bins in Subsection 4.5. Finally, we present a final discussion and the main conclusions of this study in Sections 5 and 6, respectively.

2. Data

We use the Pantheon+SH0ES compilation of SNe Ia data¹ from the analysis by Riess et al. (2022) and Brout et al. (2022). The SNe light curves covered by this compilation are fitted using the SALT2 model originally developed by Guy et al. (2010) returning parameters such as the peak magnitude in the B-band (m_B), the colour parameter defined as the difference between the magnitude in the B and V bands at the fitted epoch of peak brightness (c) and the stretch (x_1), which corresponds to a dimensionless parameter that quantifies the width of the light curve. The compilation also includes the $\log(M/M_\odot)$ and $\log(\text{sSFR yr}^{-1})$ values for each SN host galaxy, estimated from multi-band global photometry and galaxy SED fitting, as described in Scolnic et al. (2022). In addition, a covariance matrix (C) resulting from the sum of the statistical and systematic covariance matrixes including the uncertainties of supernova corrected magnitudes and distances moduli from Cepheids is also provided in the released data.

This compilation includes repeated SNe corresponding to the same event observed in different surveys which introduces non-diagonal terms for the same SN in the statistical covariance matrix representing measurement noise from components other than the light curve itself. To simplify the analysis and remove these non-vanishing off-diagonal terms, we combined the repeated observations of each SN into a single representative measurement per SN, obtaining one set of light-curve parameters c , m_B and x_1 , their corresponding uncertainties, and the covariance between them as follows. Assuming that the light curve parameters follow Gaussian distributions for each repeated observation i of a given SN j , the mean values of these parameters can be determined from the Gaussian distribution resulting from the product of all individual distributions of the repeated observations (Petersen & Pedersen 2006). The mean parameter values vector (ν_j) and the corresponding covariance matrix (Σ_j) of the

resulting distribution for a given SN j with N observations can be computed as

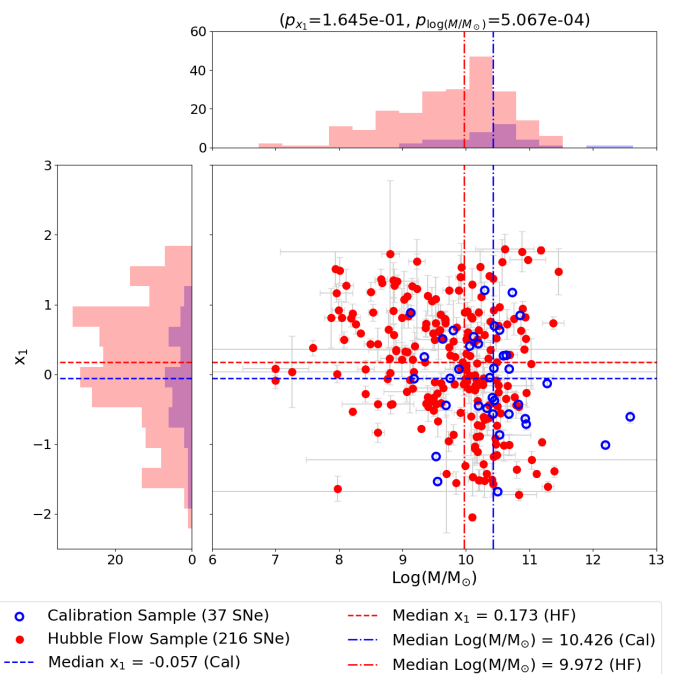
$$\nu_j = \Sigma_j \cdot \left(\sum_{i=1}^N \Sigma_i^{-1} \cdot \nu_i \right) \quad , \quad \Sigma_j = \left(\sum_{i=1}^N \Sigma_i^{-1} \right)^{-1} \quad (1)$$

where μ_i represents the mean parameter values vector for each observation i of the SN j and Σ_i the corresponding covariance matrix for that observation, both defined as:

$$\nu_i = \begin{bmatrix} m_B \\ x_1 \\ c \end{bmatrix} \quad , \quad \Sigma_i = \begin{bmatrix} \sigma_{m_B}^2 & \sigma_{m_B, x_1} & \sigma_{m_B, c} \\ \sigma_{x_1, m_B} & \sigma_{x_1}^2 & \sigma_{x_1, c} \\ \sigma_{c, m_B} & \sigma_{c, x_1} & \sigma_c^2 \end{bmatrix} \quad (2)$$

where the diagonal terms of the covariance matrix σ_{m_B} , σ_{x_1} and σ_c correspond to the uncertainties associated with each of the light curve fit parameters while the non-diagonal elements correspond to the covariance between them. All parameters defining ν_i and Σ_i for the repeated SNe are provided in the Pantheon+SH0ES compilation.

There are 7 SNe from the analysis of Riess et al. (2022) that present values of $\log(\text{sSFR yr}^{-1}) < -15$, which seem to be outliers lower limits on the true values of this parameter, which is a common interpretation in the literature (e.g., Feldmann 2017; Hahn et al. 2019). To ensure a more accurate comparison and analysis of the sSFR distributions between the two samples, we chose to retain only those with sSFR values that lie within one standard deviation (1σ) of the mean for both the calibration and Hubble Flow distributions. This treatment left us with 37 different SNe in the calibration sample and 216 SNe in the Hubble Flow sample. The light curve parameters c and x_1 and host galaxies' stellar mass (M) in solar mass units (M_\odot) and specific star formation rate (sSFR) in yr^{-1} distributions are shown in Figures 1 and 2. The redshift (z) distribution of both samples is also presented in Figure 3.



¹ <https://github.com/PantheonPlusSH0ES>

Fig. 1: Streich (x_1) as a function of the logarithm of the stellar mass (M) in solar units (M_\odot) for supernovae from both calibration (blue, open circles) and Hubble flow (red, filled circles) samples. The dashed horizontal lines correspond to the median value of the light curves parameters distributions and the dashed-dotted vertical lines to the median value of the host properties distributions for each sample depending on the colour. The K-S test p -values obtained by comparing the parameters distributions of the calibration and Hubble flow samples are also displayed at the top of the Figure.

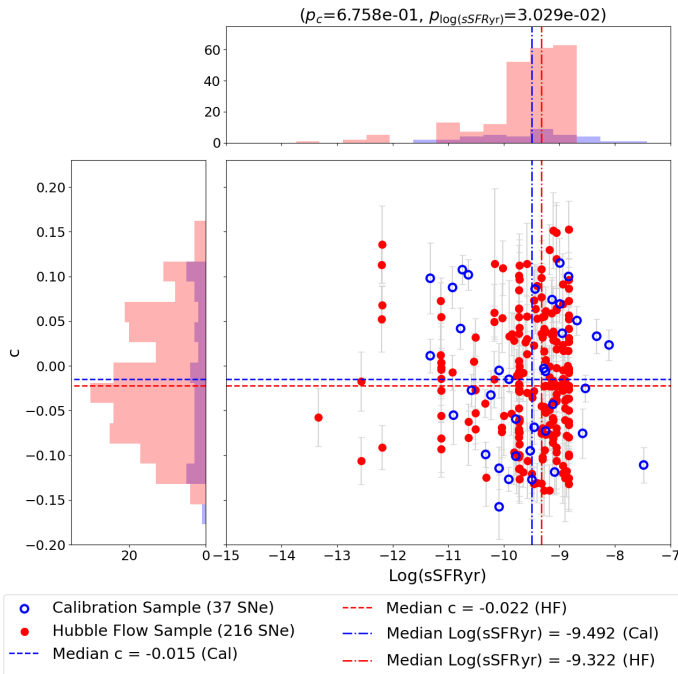


Fig. 2: Similar to Fig. 1 for colour (c) and the logarithm of the specific star formation rate (sSFR).

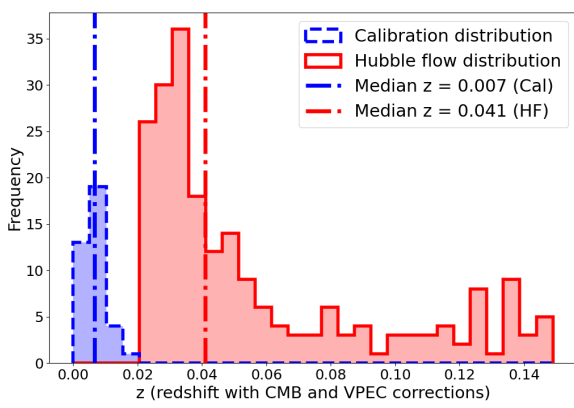


Fig. 3: Redshift (z) distribution for both calibration (blue, delineated by dashed lines) and Hubble Flow (red, delineated by solid lines) SNe samples. The redshifts are corrected for both the CMB and peculiar velocities (VPEC) and are provided in the Pantheon+SHOES compilation (Riess et al. 2022; Brout et al. 2022). The vertical dash-dotted lines indicate the redshift medians of each sample.

3. Methodology

The corrected SN magnitude using the Tripp (1998) correction model accounting for the mass step (e.g., Sullivan et al. 2010) is given by

$$m_B^{corr} = m_B + \alpha x_1 - \beta c + \delta_{host} \quad (3)$$

where α and β are the model coefficients that describe the shape-luminosity and colour-luminosity relations, respectively, while δ_{host} represents the mass step correction term depending on the SNe host stellar mass M as

$$\delta_{host} = \begin{cases} \Delta_{host} & \text{if } \log(M/M_\odot) < \log(M_{step}/M_\odot) \\ -\Delta_{host} & \text{if } \log(M/M_\odot) \geq \log(M_{step}/M_\odot) \end{cases} \quad (4)$$

with Δ_{host} corresponding to the step magnitude, M_{step} the stellar mass threshold at which the step correction is applied and M_\odot the solar mass. While most studies adopt a fixed value of $M_{step} = 10 M_\odot$, in this analysis we will set $M_{step} = \tilde{M}$, with the latter representing the median value of M for the subsamples used to obtain the parameters.

To properly account for both intrinsic and dust reddening effects on luminosity, some models assume that the observed SN colour c is the sum of two components: the intrinsic colour c_{int} , which is related to luminosity through an intrinsic colour-luminosity relation with slope β_{int} , and the colour excess due to dust, commonly referred to as dust reddening, $E(B - V)$ which is related to luminosity through the total-to-selective extinction coefficient $R_B = R_V + 1$, representing the external host-galaxy dust extinction component (Brout & Scolnic 2021). Some studies also include an additional bias correction term δ_{bias} in equation 3 to account for observational selection biases determined from simulations, as well as second order corrections arising from full forward modelling of SN colour parameters and observed magnitudes based on physically motivated models of dust and supernova intrinsic colour (e.g., Popovic et al. 2023).

By adopting a simplified β -colour correction, excluding the δ_{bias} correction term from our analysis and selecting subsamples of the calibration and HF samples that are closely matched in their properties (see Section 4), we are implicitly assuming that extinction and intrinsic colour effects are indistinguishable and identical for all SNe within the subsample. This approach avoids relying on dust and colour correction models that might not capture the full complexity of dust extinction of SNe Ia and allows us to assess the raw impact of differences in the property distributions of the calibration and Hubble flow SNe samples, as well as the effects of distinct SN subpopulations, on luminosity standardization. These effects may otherwise be overlooked by such corrections, which can themselves be incorrectly assumed to apply equally to both samples (e.g., Wojtak & Hjorth 2022, 2024).

Knowing that the distance modulus μ is defined as the difference between the standardized apparent and absolute peak magnitudes in the B-band, m_B^{corr} and M_B , and recalling the expression (3) we can define:

$$\mu = m_B^{corr} - M_B = m_B - M_B + \alpha x_1 - \beta c + \delta_{host}. \quad (5)$$

The distance modulus can also be expressed in terms of the luminosity distance $d_L(z)$, and the latter can be estimated using the Hubble parameter $H(z)$. We can then relate $\mu(z)$ for a given redshift with the local Hubble constant H_0 by expanding $H(z)$ to the first orders for low redshifts, leading to (see Peebles 2020)

$$\mu(z) \approx 5 \log_{10} \left(\frac{c}{H_0} [z + \frac{1}{2}(1 - q_0)z^2] \right) \quad (6)$$

$$- \frac{1}{6}(1 - q_0 - 3q_0^2 + j_0)z^3] \right) + 25 \quad (7)$$

with $q_0 = -0.51$ being the deceleration parameter obtained by [Riess et al. \(2022\)](#), and $j_0 = 1$ representing the jerk ([Visser 2004](#)).

To constrain the H_0 and M_B , as well as all the correction parameters α, β and Δ_{host} , we apply a Bayesian fitting procedure to minimize the value of the likelihood function described by

$$\ln(\mathcal{L}) = -\frac{1}{2} \sum_{i=0}^N [\Delta\xi_i + \ln(2\pi\sigma_i^2)], \quad (8)$$

where $\Delta\xi_i$ corresponds to the i -th component of the solution vector obtained from the system of linear equations defined for each SN i given by

$$\Delta\mu = C\Delta\xi \Leftrightarrow \Delta\xi = C^{-1}\Delta\mu \quad (9)$$

that takes into account all the covariance matrix terms and the vector $\Delta\mu$, which consists of the Hubble residuals for each SN i , defined as $\Delta\mu_i = \mu_i - \mu_{i,model}$, where μ_i is given by (5). If a SN i belongs to the calibration sample, then its distance comes from Cepheids and $\mu_{i,model} = \mu_{i,ceph}$, whereas if it is in the Hubble Flow sample we use $\mu_{i,model} = \mu_i(z)$ given by equation (7).

We have also included the Gaussian normalization term, $\ln(2\pi\sigma_i^2)$, in equation (8), as some studies (e.g., [Kessler & Scolnic 2017](#)) point out that leaving this term out from the likelihood function can introduce significant biases in the recovered fit parameters. The σ_i denotes the i -th term of the diagonal of the statistical and systematic covariance matrix C provided in the released data and is defined as

$$\sigma_i^2 = \sigma_{m_B}^2 + (\alpha\sigma_{x_1})^2 + (\beta\sigma_c)^2 - 2\beta\sigma_{m_B,c} + 2\alpha\sigma_{m_B,x_1} - 2\alpha\beta\sigma_{x_1,c} - \sigma_{int}^2 + \sigma_{lens}^2 + \sigma_z^2 + \sigma_{vpec}^2 \quad (10)$$

with σ_{m_B} , σ_{x_1} and σ_c corresponding to the uncertainties associated with the light curve fit parameters of each SN, $\sigma_{m_B,c}$, σ_{m_B,x_1} and $\sigma_{x_1,c}$ representing their covariance terms and σ_{int} being a free parameter that accounts for possible intrinsic variations in the SNe luminosities. The parameters σ_{lens} , σ_z and σ_{vpec} represent the uncertainty contribution from gravitational lensing, as given by [Jönsson et al. \(2010\)](#), and the redshift and peculiar velocity measurements uncertainties, respectively.

To constrain and estimate our own correction parameters α , β , Δ_{host} and σ_{int} that appear both in the modified Tripp formula (3) and in the diagonal terms of the covariance matrix (10), we subtracted the diagonal terms that explicitly depend on them, adopting the values of $\alpha = 1.148$ and $\beta = 3.112$ from [Brout et al. \(2022\)](#), along with the δ_{host} , σ_{int} , and covariances values between m_B , c and x_1 provided in the data compilation. We then reintroduced these terms into the covariance matrix setting the correction parameters as free parameters in the Bayesian fitting procedure that relies on the Monte Carlo Markov Chain (MCMC) technique, a sampling method used to generate distributions of values by drawing samples from a probability distribution based on independent observations implemented in the *emcee*² python

package ([Foreman-Mackey et al. 2013](#)). The parameter space was sampled using 128 walkers and 800 iterations for each fit, with an initial burn-in of 64 steps which ensures parameter convergence for all cases. For the covariance values, we used those derived during the unification of SNe parameter values, as described in Section 2.

4. Analysis

4.1. Comparing the full calibration and Hubble flow samples

To analyze and compare the light curve parameters and host properties distributions between the calibration and Hubble Flow samples we used the python implementation³ of the one-dimensional two-sample Kolmogorov–Smirnov (K–S) test provided by the SciPy library [Virtanen et al. \(2020\)](#) and introduced by [Kolmogorov \(1933\)](#) and [Smirnov \(1939\)](#). This test is used to compare two independent samples to assess whether they come from the same distribution, evaluating the maximum vertical difference between the empirical cumulative distribution functions of both. The decision is translated on the resulting p -value. If the p -value is less than the significance level of 0.05, the null hypothesis that the two samples come from the same distribution might be rejected. Otherwise, we can say that both distributions are in agreement and might come from the same distribution.

As we can see in the top of Figures 1 and 2, the x_1 and c distributions of the calibration and Hubble Flow samples seem to be in concordance with each other according to the obtained p -values of 1.645×10^{-1} and 6.758×10^{-1} , respectively. However, for the host M and sSFR distributions, we can see that the estimated p -values shown in the upper parts of both Figures are lower than 0.05, with values of 5.067×10^{-4} and 3.029×10^{-2} , respectively. This means that these properties distributions are not in agreement and most likely come from different distributions, leading us to the conclusion that SNe in the calibration sample are not representative of all the SNe found in the HF sample in terms of these two host properties. The calibration sample has no SN located in lower mass galaxies ($\log(M/M_\odot) < 9$), contrarily to the Hubble Flow sample. The calibration sample also seems to have SN hosts with $\log(\text{sSFR yr}) \gtrsim -8.8$, which are not present in the HF sample.

To estimate the Hubble constant, as well as all the other standardization parameters, we will use the approach described in Section 3. The parameters estimated using the full sample can be found in Table 1. The estimated value of H_0 is consistent with the value of $73.04 \pm 1.04 \text{ km s}^{-1} \text{ Mpc}^{-1}$ obtained by [Riess et al. \(2022\)](#), with a concordance of 0.53σ . The differences in the obtained values are likely driven by the change in the fitting methodology, the omission of bias corrections, the use of a single representative parameter value for repeatedly observed SNe, and the exclusion of certain SNe from the sample.

4.2. Comparing calibration and Hubble Flow subsamples

In order to evaluate the matching effect on the estimation of the H_0 and the correction parameters $\alpha, \beta, \Delta_{host}$ and σ_{int} we base our approach on two considerations. First, as shown in the previous Subsection 4.1, the full calibration sample is not fully representative of the HF sample in terms of stellar mass and sSFR distributions and we want to obtain more consistent properties in the calibration and HF samples. Second, there is growing evidence

³ https://docs.scipy.org/doc/scipy/reference/generated/scipy.stats.ks_2samp.html

² <https://github.com/dfm/emcee>

Sample	H_0	M_B	α	β	Δ_{host}	σ_{int}
Full Sample	$73.781^{+0.970}_{-0.944}$	$-19.199^{+0.027}_{-0.027}$	$0.136^{+0.010}_{-0.010}$	$2.777^{+0.116}_{-0.111}$	$-0.020^{+0.009}_{-0.008}$	$0.092^{+0.009}_{-0.009}$

Table 1: Median parameters values obtained using the full Calibration and Hubble flow sample and their respective difference to the 16th and 84th percentiles.

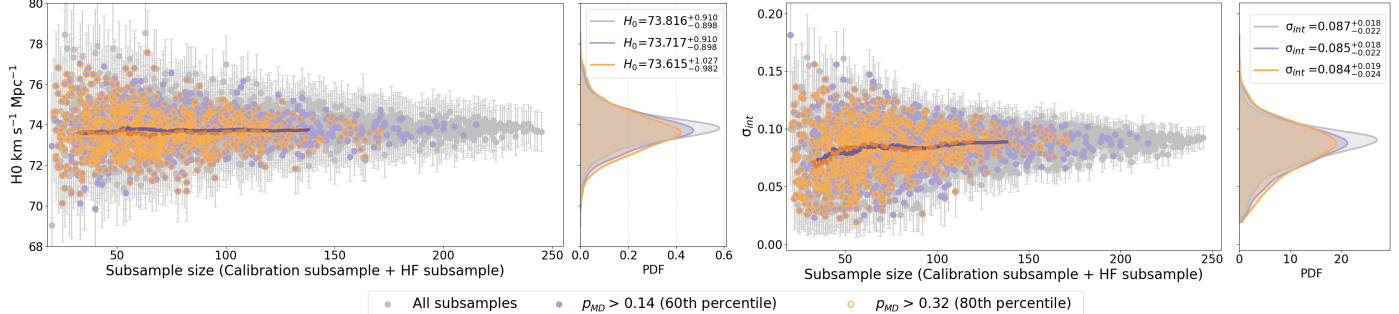


Fig. 4: H_0 (left) and σ_{int} (right) as a function of the generated subsample size, using paired subsamples drawn from the calibration and HF samples. Grey dots show the full subsample distribution, lilac dots highlight subsamples with p_{MD} above the 60th percentile, and orange open dots indicate those above the 80th percentile.

that SNe Ia have multiple subpopulations (e.g., Wang et al. 2013; Wojtak et al. 2023; Ginolini et al. 2025) that may exist even in the calibration sample. For these reasons, we generate a total of 4000 paired subsamples, each consisting of one calibration subsample and one Hubble Flow subsample. For each pair, we obtain the p -value for the c , x_1 , $\log(M/M_\odot)$ and $\log(\text{sSFRyr})$ distributions by applying the K-S test between their properties distributions, and estimated the standardization parameters for each one, as well as the H_0 to see if there is any correlation between the concordance of the distributions and the parameters estimated.

To ensure statistical significance when defining the minimum calibration subsample size, we adopted the number of SNe used in the calibration sample by Dhawan et al. (2018) to measure the H_0 as a reference, setting a lower limit of 10 SNe for each calibration subsample and an upper limit corresponding to the full calibration sample of 37 SNe. For the HF subsamples, the lower limit was set equal to the number of SNe in the corresponding calibration subsample, while the upper limit was defined as the integer part of 5.6 times that number. This factor corresponds to the approximated ratio between the total number of SNe in the full Hubble Flow sample (216 SNe) and that in the full calibration sample (37 SNe). To ensure that no subsamples were repeated, we excluded those with identical p -values for two or more of the compared distributions, resulting in 3940 unique subsamples.

In Figure 4, we present the estimated values of H_0 derived from the 3940 randomly generated subsamples. In this analysis, we use the python implementation⁴ (Chow & Brown 2025) of the multi-dimensional generalization of the two-sample K-S test described by Fasano & Franceschini (1987) to assess the overall concordance between the light curve parameters and host property distributions for each pair of generated subsamples. We refer to the latter as p_{MD} throughout this work. Other metrics are explored in appendix D showing always consistent results. We also computed the rolling median of the parameter distributions as it reduces the discrete nature of binning and provides a statistically more reliable trend than comparing medians obtained from

equally-populated or equally-spaced bins (Murakami & Scolnic 2025). Although not shown in Figure 4, the rolling median clearly confirms that there is no noticeable trend between the estimated parameters and the size of generated subsamples.

The median p_{MD} estimated for all the generated subsamples is approximately 0.097, indicating a good overall agreement between the property distributions of the calibration and HF subsamples. The H_0 values estimated using subsamples with p_{MD} above the 60th (violet circles) and 80th percentiles (orange open circles) are also shown, observing a slight reduction in the median H_0 as more consistent subsamples are used, although the values remain fully consistent within their uncertainties. No significant dependence of the estimated parameters on the subsample size is observed, with the exception of σ_{int} : as shown in the right panel of Figure 4, it tends to decrease as the subsample size becomes smaller.

We note that we also generated subsamples only from the HF sample while keeping the full calibration sample fixed. However, using this approach, most comparisons of the $\log(M/M_\odot)$ and $\log(\text{sSFRyr})$ distributions still yield low p -values, with the majority below 0.05.

4.3. Matching effect on the estimated parameters

To investigate whether a better overall match of all c , x_1 , $\log(M/M_\odot)$ and $\log(\text{sSFRyr})$ distributions between the calibration and HF subsamples affects the estimated H_0 , M_B , α , β , Δ_{host} and σ_{int} , we performed a linear regression between the obtained parameters and the logarithm of their corresponding p_{MD} . In addition, we analyzed the median values of these parameters considering only subsamples with p_{MD} above 0.05, 0.1, 0.2, 0.3, and 0.4, as illustrated in the left panel of Figure 5 for the H_0 case. While the median values of the considered parameters across subsamples with different p -value thresholds remain consistent within their uncertainties, the linear regression analysis reveals statistically significant slopes not only for H_0 which decreases with better subsample matching, but also for other parameters, as shown in Table 2.

⁴ <https://github.com/wmpg/fasano-franceschini-test>

If distinct SN Ia subpopulations exist, characterized by their stretch (e.g., Wojtak et al. 2023; Ginolin et al. 2025), and correlating strongly with their host galaxy stellar mass (e.g., Sullivan et al. 2010; Ginolin et al. 2025) and sSFR (e.g., Sullivan et al. 2010; Nicolas et al. 2021), it is possible that one the two calibration/HF samples is predominantly composed of SNe from a specific subpopulation, as suggested by Wojtak, R. & Hjorth, J. (2025). Improving thus the match in these property distributions between the calibration and HF samples could indeed influence the estimates of H_0 and M_B . The significant decrease in σ_{int} observed with improved matching of the subsamples properties further supports this interpretation. In fact, when performing the linear regression between these parameters and the one dimensional p -values obtained from comparing individually each of the c , x_1 , $\log(M/M_\odot)$, and $\log(\text{sSFRyr})$ distributions of calibration vs HF samples, we find significant slopes ($> 3\sigma$) for $\log(M/M_\odot)$ and $\log(\text{sSFRyr})$. However, the most prominent relation arises for the x_1 distributions, with significances greater than 8σ in both cases.

Parameter	Linear Regression Slope	Sig.
H_0	$(-1.485 \pm 0.217) \times 10^{-1}$	(6.84σ)
M_B	$(-4.806 \pm 0.516) \times 10^{-3}$	(9.31σ)
α	$(1.517 \pm 0.402) \times 10^{-3}$	(3.78σ)
β	$(1.113 \pm 0.422) \times 10^{-2}$	(2.64σ)
Δ_{host}	$(-7.941 \pm 3.124) \times 10^{-4}$	(2.54σ)
σ_{int}	$(-2.733 \pm 0.456) \times 10^{-3}$	(6.00σ)

Table 2: Slopes and uncertainties resulting from the linear regression between H_0 , M_B , α , β , Δ_{host} , and σ_{int} and the the logarithm of p_{MD} , along with the corresponding significance levels.

We did not find a significant relation between the mass-step magnitude term, Δ_{host} , and the increasing p_{MD} . However, when accounting for the uncertainty in the estimated parameter, we observe that the fraction of subsamples with Δ_{host} consistent with 0 within 1σ increases as the match between the property distributions improves. In fact, if we apply a linear fitting between the consistency of the mass-step magnitude with 0 given by $|\Delta_{\text{host}}/\sigma_{\Delta_{\text{host}}}|$ and the p_{MD} , we obtain a fitted slope of $(-9.998 \pm 1.694) \times 10^{-2}$ with a significance of 5.90σ , as we can see in the right panel of Figure 5. Furthermore, the probability density function (PDF) estimated for the subsamples with a multidimensional p -value greater than 0.4 shows a higher density of subsamples located in the region below 1σ consistency compared to the distribution estimated from all subsamples, and even more so compared to that of subsamples with p -values below 0.05. This trend is accompanied by a progressive decrease in the median value of $|\Delta_{\text{host}}/\sigma_{\Delta_{\text{host}}}|$ and their corresponding differences between the 16th and 84th percentiles. Specifically, the median decreases from $1.326_{-0.790}^{+0.689}$ when considering subsamples with p_{MD} lower than 0.05, to $1.092_{-0.748}^{+0.753}$ when restricting to subsamples with p -values higher than 0.4.

Nevertheless, the apparent consistency with zero observed with increasing subsample matching may also be a consequence of the reduction in subsample size. As shown in Fig. 4, better-matched subsamples tend to be associated with smaller sizes. Such a reduction is expected to enhance statistical fluctuations

and increase the associated uncertainties in the mass-step magnitude, thereby making the mass-step appear more consistent with zero due to the larger uncertainty. A more detailed discussion of the impact of subsample size on the inferred values of Δ_{host} is provided in Subsection 5.3.

4.4. Accessing SN subpopulations with random subsamples

So far, we have been testing the consistency of mixtures of populations in the calibration and in the HF subsamples, but not necessarily individual populations. Knowing that SN populations are also characterized by distinct intrinsic properties distributions (e.g., Wojtak et al. 2023), we analyze here how the estimated parameters of the most consistent subsamples vary as a function of the median values of their property distributions.

We choose to show H_0 and M_B as a function of the subsample median stretch in Figure 6, as this combination of estimated parameters and the SN light curve parameter show the strongest and most statistically significant relations. This interesting result may indicate a systematic trend where consistent subsamples, presumably composed mainly of SNe with higher x_1 , tend to yield lower values of H_0 and M_B compared to those with lower median x_1 . Moreover, the fitted slope is steeper when considering subsamples whose p -values fall within the top 20th percentile of the p -value distribution.

There is also a significant relation observed between α and $\log(M/M_\odot)$ shown in the right panel of Figure 6, and between α and $\log(\text{sSFRyr})$ with a slope of 0.021 ± 0.006 (3.55σ) and -0.021 ± 0.002 (8.83σ), respectively, when using all random subsamples. These trends may also reflect the influence of underlying SN Ia subpopulations on the luminosity standardization. Given that SN Ia stretch correlates with host galaxy properties such as $\log(M/M_\odot)$ (e.g., Sullivan et al. 2010; Uddin et al. 2017), this trend could indeed result from an incomplete stretch–luminosity correction. If this relation, normally described by a single α parameter, is not accurately represented by a simple linear model, then residual dependencies may appear in the corrected SN Ia luminosities or in the correction parameters themselves as a function of host galaxy characteristics rather than x_1 alone. Recent works by Larison et al. (2024) and Ginolin et al. (2025) support this idea, proposing a non-linear shape–luminosity correction, in contrast to the linear form adopted in the standard SN Ia calibration (equation 3). Their findings suggest that low-stretch SNe Ia follow a much steeper magnitude–stretch relation (i.e., a higher α) compared to high-stretch SNe Ia, which exhibit a weaker relation (i.e., a lower α). Considering the slope fitted for α as a function of the median $\log(M/M_\odot)$ and $\log(\text{sSFRyr})$, our results may indicate a similar effect, although less pronounced and likely mediated by the host environment.

To test whether our subsamples may indeed recover the host stellar mass and sSFR dependence with stretch, we compared the median $\log(M/M_\odot)$ and $\log(\text{sSFRyr})$ distributions of subsamples with the highest (top 10th percentile) and lowest (bottom 10th percentile) median x_1 values, as a way of increasing the likelihood of selecting subsamples predominantly composed of SNe with higher or lower stretch, respectively. Starting by the stellar mass distributions, as shown in the right panel of Figure 7, the subsamples with the lowest median x_1 tend to exhibit higher median stellar masses, with a median $\log(\tilde{M}/M_\odot) = 10.142$. This bin also shows a narrower mass distribution, as indicated by the difference between the 16th and 84th percentiles (0.162). In contrast, the subsamples with the highest median x_1 display a broader median mass distribution, spanning a wider range of

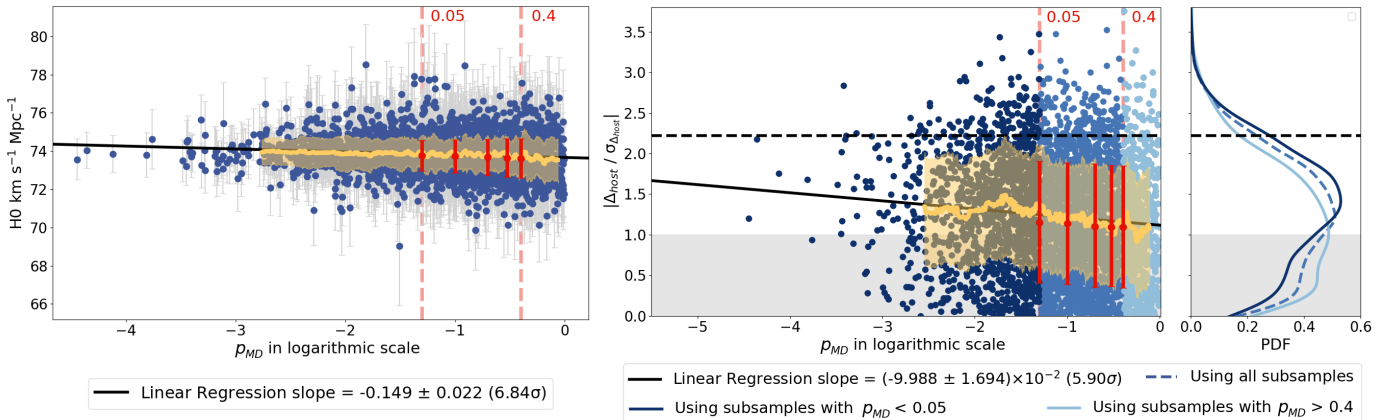


Fig. 5: Left panel: H_0 as a function of the p_{MD} obtained for each generated calibration subsample when compared to the corresponding HF subsample. The yellow line represents the rolling median of each parameter, computed using a window size of 100 subsamples, while the shaded area represents its rolling standard deviation. The red dots correspond to the median values of the parameter distribution using subsamples with p -values higher than 0.05, 0.1, 0.2 and 0.4. The red error bars indicate the difference between the 16th and 84th percentiles relative to the median values estimated for each bin. The dashed red line marks $p_{MD} = 0.05$ and $p_{MD} = 0.4$ on the logarithmic scale. Right panel: Same analysis for $\Delta_{\text{host}} / \sigma_{\Delta_{\text{host}}}$, where the dark blue dots represent subsamples with p_{MD} below 0.05, medium blue those with p_{MD} between 0.05 and 0.4, and in light blue those with p_{MD} above 0.4. The black dashed line indicates the value of $\Delta_{\text{host}} / \sigma_{\Delta_{\text{host}}}$ estimated using the full SNe sample, which is 2.22σ . The grey shaded area highlights the region where the mass-step is consistent with 0 within 1σ .

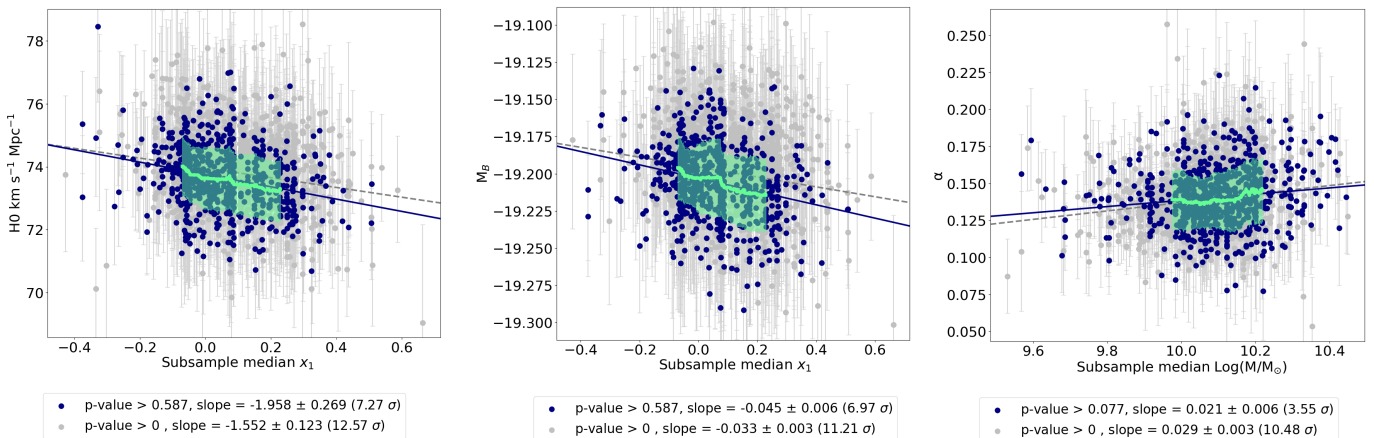


Fig. 6: Left and middle panels: Show H_0 and M_B as a function of the median value of the x_1 distribution for each generated subsample. Grey points represent all generated subsamples, each composed of one randomly drawn subsample from the calibration sample and one from the Hubble Flow sample. Blue points correspond to the best matching subsamples, defined as those whose calibration and Hubble Flow subsamples yield one dimensional p -values in the top 20th percentile when comparing their distributions in the considered property. The green line is the rolling median of the estimated parameters H_0 , M_B , and α from the best-matching subsamples, with the shaded region representing the corresponding standard deviation. Right panel: Same analysis for α as a function of the median $\log(M/M_\odot)$.

stellar masses with a percentile difference of 0.227. These subsamples also include lower median mass values, resulting in a lower median of 10.059. This finding strengthens the proposed interpretation, suggesting that the randomly generated subsamples do reflect the following trend: high-stretch SNe are found in both low- and high-mass galaxies and likely drive the lower α values measured for the low-mass hosts. In contrast, low-stretch SNe mainly occur in massive galaxies, leading to higher α values and thus a higher median of the parameter (e.g., [Ginolini et al. 2025](#)). The simultaneous presence of both populations in massive galaxies is the most probable explanation for the broader dispersion of α observed at higher stellar masses. Similar find-

ings are reported in [Garnavich et al. \(2023\)](#), showing that the estimated slopes become steeper with increasing host mass for fast-declining SNe Ia (defined in this work as $x_1 > -1$) while the α values estimated for slow-declining SNe ($x_1 < -1$) remain consistently lower and show no significant dependence on host mass.

For the sSFR, we do not observe as clear a difference in Figure 7 as we do for the stellar mass. Nevertheless, we still find that the median $\log(\text{sSFR yr})$ estimated for the subsamples with the lowest median x_1 is lower ($\log(\text{sSFR yr}) = -9.400$) than that obtained for the subsamples with the highest median x_1 ($\log(\text{sSFR yr}) = -9.322$), as also found in the literature (e.g., [Sullivan et al. 2010; Uddin et al. 2017](#)). The negative and significant

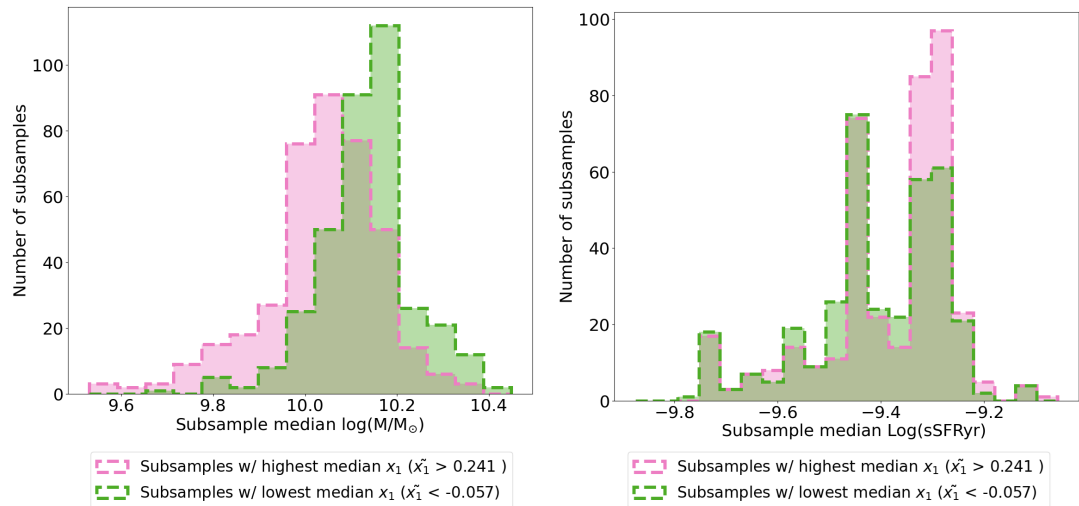


Fig. 7: Distributions of the median $\log(M/M_\odot)$ (left) and $\log(sSFRyr)$ (right) for subsamples with the highest (pink) and lowest (green) median x_1 values, restricted to those whose calibration and HF components yield one dimensional p -values in the top 20th percentile when comparing their x_1 distributions. The highest and lowest x_1 bins are defined as those in the top and bottom 10th percentiles of the full subsample median x_1 distribution, respectively.

slope found in the linear regression between α and sSFR can therefore be explained by a similar environmental dependence as that reported for stellar mass, since SNe with lower stretch tend to occur in less star-forming galaxies, while higher-stretch SNe are found in galaxies with higher sSFR (e.g., Sullivan et al. 2010; Uddin et al. 2017; Larison et al. 2024). This correlation can explain the decrease of the stretch–luminosity slope parameter with increasing $\log(sSFRyr)$. Despite the observed trends between the α parameter and the median environmental properties values typically associated with the different x_1 SN subpopulations, it remains surprising that no significant relation is observed with the median x_1 itself, for which a slope of -0.005 ± 0.002 (2.24σ) is obtained.

A significant slope of 1.313 ± 0.148 (8.86σ) is found when applying a linear regression between H_0 and $\log(M/M_\odot)$ using all subsamples, becoming even steeper when only the more consistent subsamples are considered (1.426 ± 0.318). Although this trend could also reflect the influence of underlying SN subpopulations characterized by the x_1 parameter and their dependence on stellar mass, it is also important to note that lowering the median $\log(M/M_\odot)$ effectively reduces the mass-step threshold defined for that subsample, which in turn can lead to a reduction of the mass step itself (see Figure 6 from Duarte et al. 2023). Indeed, we estimate a significant negative slope of -0.014 ± 0.002 (6.77σ) when comparing Δ_{host} with the median $\log(M/M_\odot)$, capturing this effect and likely contributing to the relation observed between H_0 and host stellar mass. However, when comparing our lower median value of $\log(M/M_\odot) = 9.53$ with the stellar mass interval explored in Duarte et al. (2023), the reduction in step magnitude relative to both the threshold yielding the most significant step ($\log(M/M_\odot) = 9.73$) and the threshold commonly adopted in the literature ($\log(M/M_\odot) \approx 10$) (e.g., Beteoule et al. 2014; Johansson et al. 2021) appears nearly negligible, as all stellar mass thresholds above our minimum median $\log(M/M_\odot)$ seem to result in consistent step magnitudes. Therefore, this effect should not significantly impact our results and may reflect the influence of the mixed underlying SN subpopulations contributing to the origin of the mass step, as discussed in Section 5.4.

The relations involving other standardization parameters, as well as those involving different light-curve and host-galaxy properties, are much less clear, showing at most weak or marginal dependencies.

4.5. Accessing SN subpopulations through property binning

In order to minimize differences in the properties of SNe within and between the calibration and HF subsamples and thereby reduce the probability of including SNe from different subpopulations within the same random subsample, we divide the full calibration and HF samples into two distinct bins of SNe for each considered property, using the median value of that property distribution across the full sample as the dividing threshold. We then compare the values of H_0 , M_B , α , β , Δ_{host} and σ_{int} estimated using all the SNe from each bin. The median values obtained for each property were $\tilde{c} = -0.022$, $\tilde{x}_1 = 0.087$, $\log(\tilde{M}/M_\odot) = 10.019$ and $\log(\tilde{sSFRyr}) = -9.322$.

The most notable discrepancies are observed between the low- and high-stretch bins, with differences of 2.00σ in H_0 and 2.23σ in M_B when using the entire sample, as shown in Table 3. In contrast, bins defined by other properties such as c , $\log(M/M_\odot)$ and $\log(sSFRyr)$, show much smaller variations in both parameters, with differences remaining below 0.84σ . No other notable variations are found in the estimated parameters across the different bins of any other property, with all results remaining highly consistent. Interestingly, in both stretch bins, the mass step is consistent with zero within approximately 1σ uncertainties, with $\Delta_{\text{host}} = -0.016 \pm 0.012$ (1.29σ) for the low-stretch bin and $\Delta_{\text{host}} = -0.012 \pm 0.012$ (1.00σ) for the high-stretch bin, a behavior that is not observed for any other parameter. A complete summary of all parameters estimated using this approach, along with the corresponding discrepancies, is provided in Tables 5 and 6. The choice of the median as a separation between both stretch samples is not necessarily ideal; however as shown in appendix B, this choice does not affect our main results.

When comparing each property distribution between the calibration and HF samples in both stretch bins using the K-S test, we still find that the $\log(M/M_\odot)$ distribution of the calibration

Division value	Lower stretch bin				Higher stretch bin			
	c	x_1	$\log(M/M_\odot)$	$\log(\text{sSFRyr})$	c	x_1	$\log(M/M_\odot)$	$\log(\text{sSFRyr})$
\tilde{x}_1	0.986	0.763	0.007	0.259	0.417	0.198	0.048	0.094

Table 4: Estimated p -values by comparing the calibration and HF sample properties distributions for each stretch bin under the defined binning threshold of $\tilde{x}_1 = 0.087$.

sample is not fully representative of that of the HF sample in both stretch bins, as shown in table 4. Overall, the calibration and HF samples in the low-stretch bin exhibit a higher level of consistency than those in the high-stretch bin for the remaining properties. Furthermore, when applying the multi-dimensional adaptation of the K–S test, the resulting p_{MD} fall below the significance threshold for the high-stretch mode, yielding a value of 0.025.

To ensure that the calibration and HF samples are well matched within each stretch bin, we follow the same approach as in Subsection 4.2 and generate 600 random SNe subsamples⁵ from the calibration and Hubble Flow samples within each stretch bin to investigate how the improved matching of their property distributions affects the estimated parameters.

SNe bin	Number of SNe	H_0	M_B
$x_1 < \tilde{x}_1$	126	$75.266^{+1.191}_{-1.166}$	$-19.155^{+0.033}_{-0.033}$
$x_1 \geq \tilde{x}_1$	127	$71.247^{+1.638}_{-1.546}$	$-19.293^{+0.052}_{-0.051}$

Table 3: Estimated H_0 and M_B using SNe from two different bins divided by the median $\tilde{x}_1 = 0.087$, and their respective difference to the 16th and 84th percentiles. The number of SNe in each bin is also provided.

As shown in the left panel of Figure 8, we find a significant discrepancy of 3.30σ between the median value of H_0 derived from the high-stretch subsamples and that obtained from the low-stretch subsamples. However, this difference do not seem to become more significant with the increasing of the p_{MD} . For the M_B parameter, we also identify a notable difference of 2.90σ , which do not seem to increase with the better overall matching of the calibration and HF subsamples, as well. The other estimated parameters remain consistent across subsamples, with differences below the 1σ level, without showing any relation with the increasing p_{MD} .

When we look to the mass-step magnitudes estimated for both stretch bins and their corresponding uncertainties, we observe that the majority of the subsamples drawn from both stretch bins give Δ_{host} values consistent with 0 under a 1σ difference, independently of the better matching of the calibration and HF subsamples properties, as illustrated in the right panel of the Figure 8. In this case, both stretch modes present a mass step consistent with 0 within approximately 1σ uncertainties, obtaining $\Delta_{\text{host}} = -0.015 \pm 0.013$ (1.15σ) for the low-stretch mode and $\Delta_{\text{host}} = -0.015 \pm 0.014$ (1.07σ) for the high stretch mode. All

⁵ This number of subsamples is sufficient for robust statistics. The number of combinations that are significantly different is limited, given the small difference between the minimum number of 10 SNe per subsample and the 14 calibrators in the high-stretch bin, and we expect relatively little mixing of SN subpopulations within each bin. Hence, increasing the number of subsamples would likely not substantially affect the results.

parameters estimated using this approach, along with the corresponding discrepancies, are shown in tables 7 and 8.

From our analysis, the largest and most significant differences in the estimated H_0 and M_B parameters between low- and high-stretch SNe primarily arise from the absence of additional bias correction terms (Popovic et al. 2023) and the neglect of a differentiation of the observed colour into intrinsic and dust extinction (Brout & Scolnic 2021). By doing so, we are assuming that all SNe are intrinsically similar and that the dust extinction law (characterized by R_V) is consistent for all samples, with dust reddening affecting SN colours in the same way for all events. The significantly lower H_0 and M_B values estimated using slow-declining (high-stretch) vs fast-declining (low-stretch) SNe suggest that these subpopulations may have intrinsic colour variations or dust extinction differences that are not properly corrected with the simple Tripp standardization law. A more detailed interpretation and discussion of these results, as well as of the discrepancies identified between the different SNe bins, is provided in 5.1, where we also compare our findings with previous results in the literature.

Regarding the mass step, the fact that Δ_{host} is repeatedly found to be consistent with zero within approximately 1σ uncertainty when the SN subpopulations are considered separately, contrary to the 2.22σ deviation from zero obtained using the full sample, indicates that the mass step might arise from an over-correction of more than one subpopulation with different properties occurring in different environments which are not distinguished in the full SN sample. An additional noteworthy result that supports this conclusion is that all parameter estimates for the two stretch bins can be recovered without fitting the mass-step term. Nevertheless, it could be argued that the apparent consistency with zero could also be an effect of reducing the subsamples sizes, as noted in Subsection 4.2. A more detailed discussion of the impact of subsample size on the inferred values of Δ_{host} , as well as on the possible origin of the mass step, are provided in Subsections 5.3 and 5.4, respectively.

In appendix C, we present alternative approaches for distinguishing the different SN subpopulations, along with the parameters derived for each stretch mode. These include adopting a different division threshold in the stretch distribution to improve the consistency of property distributions between the calibration and Hubble flow subsamples within each bin, as well as using a Gaussian Mixture Models (GMM) based clustering algorithm to distinguish both SN subpopulations.

5. Discussion

5.1. Effect of the SN subpopulations

The H_0 and M_B discrepancies observed for the $\log(M/M_\odot)$ and $\log(\text{sSFRyr})$ bins, seem to be simply reflecting the effect of the underlying SNe subpopulations presented and partially identified throughout this study, which are essentially separated and identified by the stretch parameter x_1 .

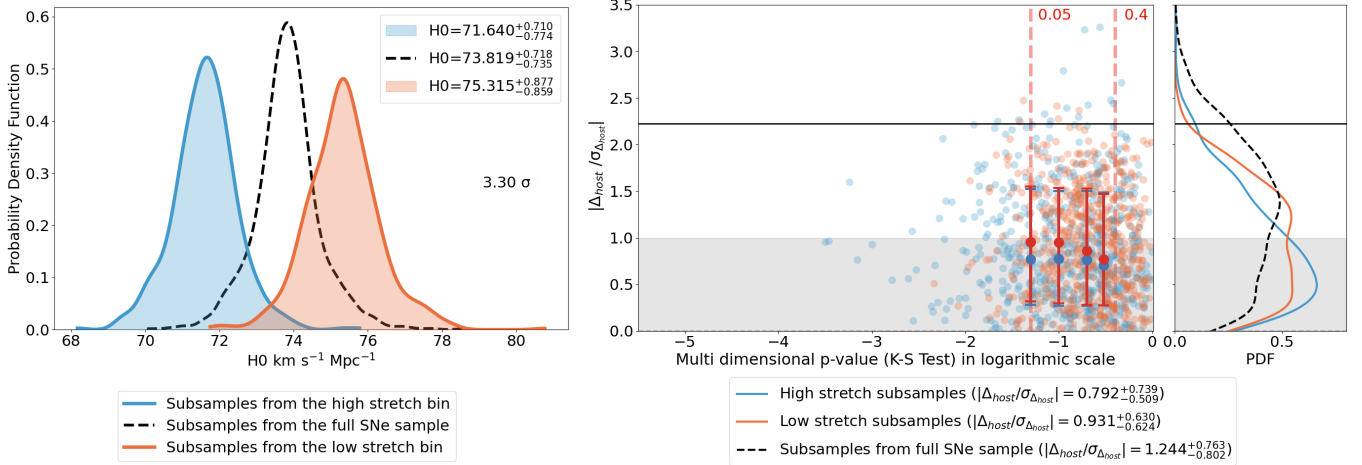


Fig. 8: Left panel: Probability density function (PDF) of the H_0 distribution estimated from SNe subsamples in the higher-stretch (blue) and lower-stretch (orange) bins defined using $\tilde{x}_1 = 0.087$. Right panel: Same analysis as in the right panel of Figure 5, with the orange dots representing subsamples drawn from the lower-stretch bin and blue dots representing those from the higher-stretch bin. Median values and corresponding uncertainties are not shown for subsamples with $p_{MD} > 0.4$ due to the low number of subsamples in that region for the low stretch bin. In both panels, the black dashed lines represent the H_0 and $\Delta_{\text{host}}/\sigma_{\Delta_{\text{host}}}$ PDFs estimated from the subsamples generated in Section 4.2 using the full SN sample.

SNe with higher stretch can be associated with both redder and bluer environments, and with both more and less massive hosts. They are also typically linked to star forming environments. In contrast, SNe with lower stretch are mainly associated with redder, high-mass galaxies with lower sSFR (e.g., [Ginolini et al. 2025](#); [Uddin et al. 2017](#); [Neill et al. 2009](#)). As shown in Table 5, the bin composed of SNe hosted in less massive galaxies (typically with higher x_1) yields a lower H_0 compared to the bin that includes SNe from more massive galaxies (with both high and low x_1 SNe). Similarly, we can see in the same Table that the Hubble constant estimated using SNe in more actively star-forming galaxies is lower than the one estimated using SNe from galaxies with lower sSFR.

We can also detect a 1.11σ difference when comparing the H_0 obtained using SNe in different colour bins, with the bluer SNe giving a lower value of H_0 . The empirical shape-luminosity ([Phillips 1993](#)) and colour-luminosity ([Tripp 1998](#)) relations imply that intrinsically brighter SNe Ia are bluer and have slower declining lightcurves (higher stretch). According to [González-Gaitán et al. \(2021\)](#), bluer SNe Ia are consistent with a lower colour-luminosity parameter β , contrary to redder SNe. This result is also recovered in this study, as we can see in Table 6, obtaining a difference of 1.10σ between the β estimated using redder SNe and bluer ones. This can be explained with β being a combination of a low intrinsic colour-luminosity relation dominant in bluer SNe and a higher extrinsic reddening relation dominant at redder colours.

In the same study ([González-Gaitán et al. 2021](#)), the authors also suggest that bluer SNe in low-mass galaxies are the most homogeneous sample, with lower intrinsic scatter than the redder SNe. Multiple studies also suggest less intrinsic scatter in local star-forming environments (e.g., [Rigault et al. 2013](#)), as well as in global star-forming hosts (e.g., [Kelly et al. 2015](#); [Uddin et al. 2017](#)). Given that intrinsically bluer SNe seems to occur in low-mass galaxies (e.g., [Pan 2020](#)), less luminosity scatter for blue SN colours in low-mass and higher local star-forming environments may partly be associated to the higher stretch-mode subpopulation of SNe, as this is the dominant subpopulation in

low-mass environments and strongly associated to higher local sSFR (e.g., [Rigault et al. 2020b](#)). The authors suggest that red SNe probably have larger luminosity scatter from a mixture of both a different intrinsic colour population and a larger extinction, not easily corrected with a simple linear colour-luminosity relation. [Kelsey et al. \(2022\)](#) also observe the lowest scatter in the Hubble residual (HR) for blue SNe in low mass and blue environments, which coincides again with the subpopulation of SNe with the highest stretch. Despite previous reports in the literature, our study finds no significant difference in the intrinsic scatter σ_{int} between the low- and high-stretch bins. This consistency holds even though we did not divide the SNe sample by stretch and colour, or by any environmental property and colour.

According to [Wojtak et al. \(2023\)](#), SNe from the population with higher average x_1 are found to be intrinsically bluer ($c \approx -0.11$) and twice as reddened by dust than those from the other population which is dominated with $c \approx -0.04$. Although we do not have the intrinsic colour of the SNe, directly using the observable colour c , we can deduce from the cited studies that bluer SNe are the ones that are less affected by the dust reddening and thus more homogeneous between them, with the observable colour closer to the intrinsic one. As we can see in Figure 9, a small difference between the median colour of the SNe from the high stretch bin can be seen when compared to the ones with lower stretch. However, we need to take into account that we can still have higher stretch SNe (presumably intrinsically bluer) in higher mass environments that will be observed with a redder colour due to the dust reddening (e.g., [Conley et al. 2007](#); [Duarte et al. 2023](#)), limiting the ability to distinguish the two SN subpopulations based only on the observed colour.

For the stretch-luminosity relation slope α , we do not observe any significant differences between the estimated values across the bins of any property, contrary to the differences found in other studies (e.g., [Garnavich et al. 2023](#); [Larison et al. 2024](#); [Ginolini et al. 2025](#)). The differing levels of significance reported in these studies compared to our work can primarily be attributed to variations in binning criteria and the methodological

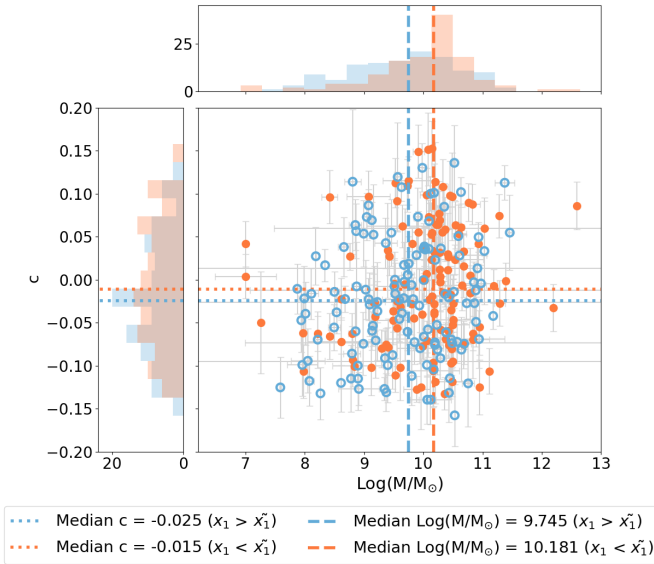


Fig. 9: Colour (c) as a function of $\log(M/M_\odot)$ for SNe from both the lower stretch bin (orange) and higher stretch one (blue) divided by the median stretch \tilde{x}_1 . The dotted horizontal lines correspond to the median value of the c distributions and the dashed vertical lines to the median value of the $\log(M/M_\odot)$ distributions for each sample depending on the colour

approaches adopted across the studies, as well as to the smaller SNe sample size used in our study.

In the first two works by Garnavich et al. (2023) and Larson et al. (2024), the authors classify SNe Ia into fast-declining (lower x_1) and slow-declining (higher x_1) populations using a fixed threshold at $x_1 = -1$. Within each bin, they perform a weighted linear regression on the colour-corrected absolute magnitudes, adopting a fixed β value, and model the dependence on x_1 independently for the two regimes. In contrast, in Golinlin et al. (2025) the authors employ a broken- α standardization model aimed at reducing Hubble residuals. This approach introduces two distinct shape-luminosity slope parameters for the different stretch regimes and simultaneously fits the breaking point separating the two x_1 modes, as well as all other correction parameters included in the standardization formalism of Tripp (1998). However, the largest difference in the median values of α is found between the x_1 bins, whose associated uncertainties also span a much wider range compared to those obtained using SNe from bins of the other properties. Interestingly, when the lower and higher stretch bins are defined using SNe with x_1 values below the 30th percentile and above the 50th percentile of the full stretch distribution, thereby reducing the overlap of stretch distributions between subpopulations in each bin, the difference in the estimated α between the two bins becomes larger, but still consistent with 0.77σ .

At the end of Section 4.5, we concluded that the most significant differences in the estimated H_0 and M_B parameters between low- and high-stretch SNe primarily arise from the absence of additional bias correction terms (Popovic et al. 2023) and the neglect of any intrinsic or dust reddening effects in our luminosity corrections (Brout & Scolnic 2021). When we apply a simplified colour-luminosity correction defined by a single β parameter, we assume that extinction and intrinsic colour effects are indistinguishable and identical for all SNe, which does not appear to be the case (e.g., González-Gaitán et al. 2021). By defining

different SN bins according to their stretch, we assume that SNe within each bin are more likely to be intrinsically similar and that the dust extinction law (characterized by R_V) is more consistent within each bin. However, if this assumption is not true, an incorrect dust correction from the β -colour relation that is not properly accounting for inconsistent dust properties between the calibration and HF samples within the same stretch bin, can cause the systematically higher H_0 and M_B values obtained for the lower-stretch SNe bins defined in the previous Sections.

In Figure 10, we estimate H_0 separately for the low- and high-stretch bins, while fixing β to different values. All other parameters are left free, except for the mass-step magnitude (Δ_{host}), which is fixed to 0.

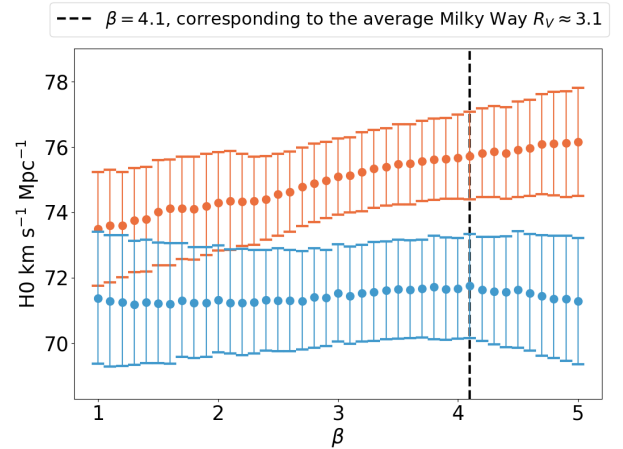


Fig. 10: H_0 as a function of the fixed β value, estimated separately for the low-stretch (orange) and high-stretch (blue) SN bins defined with $\tilde{x}_1 = 0.087$. The black dashed line indicates the value of β expected for the Milky Way dust law if the colour-luminosity relation were driven solely by dust.

If the colour-luminosity relation were driven solely by dust, then we would expect to have $\beta \approx R_V + 1$. In this scenario, a value of $\beta \approx 1$ would correspond to a very low R_V and both stretch bins would be expected to respond similarly to variations in β , since changes in this parameter would directly correspond to changes in R_V . However, β also includes a contribution from intrinsic colour variations, given by β_{int} . Therefore, if one stretch bin has relatively uniform dust properties (i.e., a well-defined R_V), changes in the fixed β will have a smaller effect on its corrected luminosities and, consequently, on H_0 . On the other hand, if one stretch bin contains SNe with more diverse or inconsistent dust properties (or alternatively a set of varying intrinsic colours), its inferred H_0 will be more sensitive to changes in β . This is exactly what we observe in Figure 10. The value of H_0 inferred from the high-stretch bin does not show a strong dependence on the choice of the fixed β parameter. In contrast, the low-stretch bin exhibits a much more pronounced variation, with H_0 decreasing as β decreases. This behavior is consistent with the low-stretch population having more heterogeneous dust properties (or more heterogeneous intrinsic colour properties), while the high-stretch population appears to be more uniform in both its dust characteristics and intrinsic colour. This differing behavior between the two stretch populations, not only in the inferred values of H_0 and M_B but also in their response to changes in the β parameter, points to clear intrinsic and/or dust differences between the populations.

More recently, [Wojtak, R. & Hjorth, J. \(2025\)](#) probabilistically separated high-stretch and low-stretch SN Ia populations, and independently constrained the supernova and extinction properties within each population. They found that the calibration sample is consistent with being composed entirely of supernovae from the younger (high-stretch) population, which naturally results from the selection of late-type, star-forming host galaxies for Cepheid observations. In contrast, the Hubble flow sample exhibits a bimodal x_1 distribution, reflecting the presence of two underlying SN Ia populations that differ primarily in their mean absolute magnitudes M_B and total-to-selective extinction coefficients R_B . The authors estimate a mean R_B for the young population that is consistent with the typical Milky Way value of $R_B \approx 4.3$ (e.g., [Fitzpatrick & Massa 2007](#)), suggesting that the dust properties in this population, and thus in the calibration sample, are similar to those observed in the Milky Way. In contrast, the older population exhibits a lower value of $R_B \approx 3$, indicating a mismatch in the sample's dust properties. This is consistent with our findings, as we observe a significant difference in the estimated absolute magnitude between the two subpopulations distinguished by stretch ($\Delta M_B \approx 0.108$) and since we do not apply corrections based on intrinsic colour variations or dust extinction models, our results suggest that the higher-stretch (younger) subpopulation exhibits more homogeneous dust properties compared to the lower-stretch (older) subpopulation.

5.2. Effect of SN subpopulations on the H_0 uncertainty

Generating subsamples from the higher and lower stretch SN bins defined in Subsection 4.5, regardless of the size of the calibration or HF subsamples, reveals a substantial difference between the H_0 distributions estimated for each bin, as we can see in Figure 11. This suggests that the broad H_0 distribution observed in Figure 4 when generating subsamples may primarily result from partially sampling different SN subpopulations present in both the calibration and Hubble Flow samples, which produce consistently distinct H_0 distributions, rather than from statistical fluctuations caused solely by the reduced subsample sizes.

Since the subsamples are generated randomly, most contain SNe from both subpopulations, even though some can present a higher fraction of SNe from one specific SN subpopulation, leading to a higher or lower \tilde{x}_1 . The mixing of SN subpopulations in the generated subsamples can cause the two H_0 distributions observed in the left panel of Figure 11 to partially overlap, producing a single broader Gaussian shaped distribution. If we generate SN subsamples from the different x_1 bins divided by the median stretch of the full sample distribution ($\tilde{x}_1 = 0.087$), but replace one third of each subsample with SNe drawn from the opposite stretch bin, the discrepancy between the resulting distributions is reduced, with the H_0 distributions from both bins starting to become more disperse and to overlap, as we show in the right panel of the same figure, resembling the PDF obtained in the Figure 4. For that reason, if both underlying SN subpopulations are present in the SNe sample from which we estimate a single value of H_0 , the associated uncertainty should be increased relative to the values typically reported in the literature.

When we treat the two stretch subpopulations separately and generate subsamples within each bin, the uncertainty in the inferred Hubble parameter increases significantly. In this case, we obtain $H_0 = 73.453^{+2.453}_{-2.166} \text{ km s}^{-1} \text{ Mpc}^{-1}$ (as shown in the left panel of figure 11), with a 2.4 times larger uncertainty than the one obtained using all subsamples generated from the full SN sample, for which we obtain $H_0 = 73.816^{+0.910}_{-0.898} \text{ km s}^{-1} \text{ Mpc}^{-1}$

(grey dots in the left panel of Figure 4). It is also about 2.3 times larger than the uncertainty estimated using the full SN sample, with $H_0 = 73.781^{+0.970}_{-0.944} \text{ km s}^{-1} \text{ Mpc}^{-1}$ (see Table 1). If we adopt the larger uncertainty obtained when treating the subpopulations independently as the true uncertainty of the full SN sample H_0 estimate, we obtain $H_0 = 73.781 \pm 2.166 \text{ km s}^{-1} \text{ Mpc}^{-1}$. Under this assumption, the tension with the [Planck Collaboration et al. \(2020\)](#) measurement would be reduced from approximately 5.87σ to about 2.86σ .

Although we do not perform a direct comparison between the uncertainties estimated for H_0 in this study (where we consider the separate contributions of the two SN subpopulations characterized by x_1) and those reported in other works such as [Riess et al. \(2022\)](#), due to methodological differences, we emphasize that the contribution of both underlying SN subpopulations should be treated more carefully in future determinations of H_0 uncertainties.

5.3. Effect of Subsample Size on the Mass Step

As concluded in Sections 4.2 and 4.5, the mass-step magnitude tends to become more consistent with 0 as the overall matching between the calibration and HF subsamples improves, becoming effectively consistent with zero when SNe are analyzed separately by stretch mode. However, this apparent consistency may also partially reflect the reduction in subsample sizes, which can increase statistical fluctuations and the associated uncertainties in the mass-step magnitude.

Figure 4 shows that subsample matching generally improves as subsample sizes decrease. To assess whether correlation between these variables affects their individual relation with the $\Delta_{\text{host}}/\sigma_{\text{host}}$ parameter, we computed their Variance Inflation Factor (VIF), which quantifies how much the variance of a regression coefficient is inflated due to correlation with other predictors (see [Marquardt 1970](#)). Both the p_{MD} and subsample size yielded a VIF of ~ 1.2 , indicating that their contributions to the observed trend in $\Delta_{\text{host}}/\sigma_{\Delta_{\text{host}}}$ are largely independent. Consequently, the trend of the mass-step magnitude approaching zero with increasing p_{MD} is not simply a proxy for the effect of subsample size.

We then modeled $\Delta_{\text{host}}/\sigma_{\Delta_{\text{host}}}$ as a linear combination of the p_{MD} and subsample size using the Ordinary Least Squares (OLS) approach. The estimated coefficients indicate that the effect of subsample size, $(6.6 \pm 0.2) \times 10^{-3}$, is much more significant ($\sim 30\sigma$) than that of the p_{MD} , 0.30 ± 0.05 ($\sim 6\sigma$). Overall, these results suggest that subsample size exerts a substantially stronger influence on $\Delta_{\text{host}}/\sigma_{\text{host}}$ than improved subsample matching, although both are significant. While the trend observed in the right panel of Figure 5 is not purely a proxy effect of subsample size, we cannot completely rule out a minor contribution, since selecting subsamples with higher p_{MD} tends to favor smaller subsample sizes.

Interestingly, the R^2 obtained from this fitting shows that these two variables together explain only $\sim 19\%$ of the variance in the mass-step consistency. Considering the results from Subsections 4.5 and 4.5, the specific properties of the SNe composing each subsample likely contribute significantly to the observed variation in $\Delta_{\text{host}}/\sigma_{\Delta_{\text{host}}}$. For instance, subsamples dominated by SNe with either higher or lower stretch are more likely drawn from the same SN subpopulation, yielding a mass step closer to zero. This could explain the absence of a significant linear correlation between Δ_{host} and the subsample median stretch observed in Subsection 4.4. On the other hand, the significant correlation between the median $\log(M/M_\odot)$ and Δ_{host} in the same Subsection supports this interpretation. Subsamples with lower

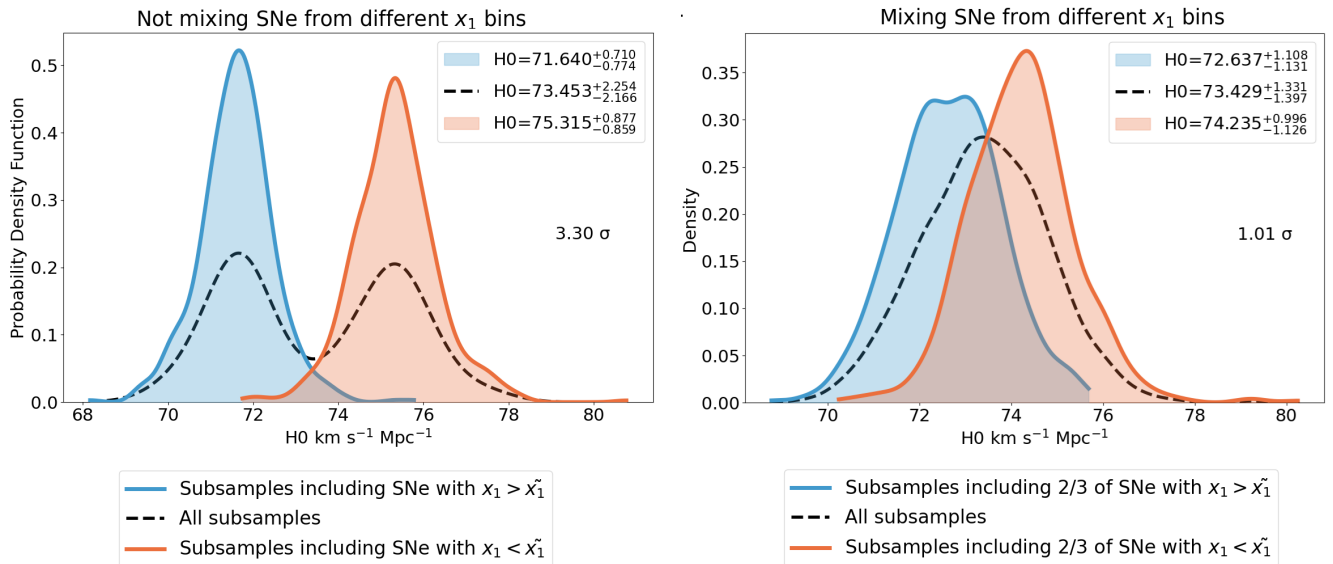


Fig. 11: The left panel shows the probability density function of the H_0 distribution from subsamples containing only SNe with x_1 above (blue) or below (orange) the median stretch value for the full sample distribution \tilde{x}_1 , along with the total distribution from all subsamples (black dashed). The right panel shows the corresponding distributions when subsamples include 2/3 of SNe from one stretch bin and 1/3 from the opposite bin. In both cases, the discrepancy between the median H_0 values of the lower and higher stretch distributions is shown at the top of the plot.

median stellar mass are less likely to contain SNe from multiple subpopulations and more likely to be dominated by higher-stretch SNe (see right panel from Figure 7), resulting in Δ_{host} values closer to zero.

5.4. Mass-step possible origin

Some studies have suggested that the observed mass step in SNe Ia luminosities may originate from the dust properties of their host galaxies. For instance, Brout & Scolnic (2021) find that the correlation between the corrected luminosity and the host galaxy mass can be attributed to differences in the ratio of total-to-selective attenuation (R_V) values between low- and high-mass galaxies. More recently, Wiseman et al. (2023b) reported that the variation of R_V with galaxy age can explain almost the entire observed mass step. Since the stellar mass of a galaxy seems to be correlated with the population age (e.g., Kang et al. 2016), the host mass step may instead reflect a progenitor age effect on the standardized brightnesses of SNe Ia (e.g., Kang et al. 2020; Lee et al. 2020) rather than being mainly influenced by dust. Indeed, there is evidence to suggest that the mass step cannot entirely be explained as a dust systematic (e.g., Uddin et al. 2020; González-Gaitán et al. 2021; Ponder et al. 2021; Thorp & Mandel 2022; Duarte et al. 2023).

In Chung et al. (2023) the authors suggest that the mass step arises from the bimodal nature of the host galaxies age distribution, based on the empirical galaxy colour–magnitude relation. Some studies have been reporting strong correlations between post-standardization SN Ia luminosities and their progenitor age (e.g., Lee et al. 2022; Chung et al. 2025), with the implicit assumption that the stellar population from which the SN progenitor originated shared these global properties, including the stellar population age. Some studies have shown that the sSFR measured locally to the SN is a relatively pure tracer of the progenitor age (e.g., Wiseman et al. 2023b) and that locally star forming

environments are fainter after standardization than those from locally passive environments, suggesting that this luminosity step manifests itself most strongly when using the local SFR at the SN location, rather than the global SFR or the stellar mass of the host galaxy (e.g., Rigault et al. 2015; Kim et al. 2018).

Interestingly, and as already introduced and discussed in Subsection 5.1, the bimodal behavior of the x_1 distribution is found to be associated with the presence of underlying populations of SNe with dependence on environment-based progenitor age (e.g., Rigault et al. 2015; Nicolas et al. 2021), with higher stretch SNe being associated to higher local sSFR environments and younger progenitors, contrary to the lower stretch population (e.g., Rigault et al. 2020b). Not only with the star formation rate, but these SN populations also seem to be strongly correlated with their host galaxies masses, with less massive galaxies mostly hosting SNe with higher stretch, and the more massive galaxies hosting SNe from both stretch modes (e.g., Sullivan et al. 2010; Ginolini et al. 2025).

As shown across Section 4, low-stretch SNe, typically associated with more massive hosts and older progenitors, are intrinsically fainter ($M_B \approx -19.167$ mag) than high-stretch SNe, which are linked to younger progenitors and occur in both low- and high-mass galaxies ($M_B \approx -19.275$ mag), yielding a difference of ~ 0.108 mag and a mass step magnitude consistent with 0. Assuming all other correction parameters are consistent, we should expect that low-mass hosts dominated by the high-stretch subpopulation host SNe Ia would appear fainter, while high-mass hosts containing both subpopulations would host SNe that appear brighter after standardization, due to the inaccurate assumption of a universal SNe Ia intrinsic brightness. This suggests that the mass step may arise from an over-correction of more than one subpopulation with different properties occurring in different environments, in an attempt to account for their intrinsic absolute magnitude differences rather than treating the subpopulations separately. Some studies such as the ones by Rigault et al.

(2013) and Childress et al. (2014), and more recently Rigault et al. (2020b), also point that the stellar mass bias is, at least, partially caused by this local sSFR and, consequently, progenitor age bias.

On the other hand, as discussed in Section 5.1 and reported in other studies such as Wojtak et al. (2023) and more recently Wojtak, R. & Hjorth, J. (2025), SN subpopulations can also be associated with different mean total-to-selective extinction coefficients. The high-stretch SN subpopulation tends to yield higher mean R_B values, closely matching the mean value estimated for the Milky Way ($R_B = R_V + 1 \approx 4$) (e.g., Fitzpatrick & Massa 2007; Schlafly et al. 2016), while the low-stretch subpopulation appears to be associated with lower R_B values. Brout & Scolnic (2021) predict that SNe in lower-mass galaxies have, on average, higher R_V (and thus R_B) values than those in higher-mass galaxies. Similarly, Salim et al. (2018) found that quiescent galaxies, typically more massive, have a mean R_V of 2.61, while star-forming galaxies, which are on average less massive, have a mean $R_V = 3.15$. These trends are consistent with the host environmental dependence observed for each SN subpopulation characterized by their stretch parameter (e.g., Sullivan et al. 2010; Ginolini et al. 2025) and linked to progenitor age (e.g., Rigault et al. 2020b) and, consequently, to the progenitor channel (e.g., Brandt et al. 2010).

Both SN subpopulations associated with different R_V values (e.g., Wojtak, R. & Hjorth, J. 2025) can be found in more massive galaxies, potentially increasing the average total-to-selective extinction coefficient. In less massive galaxies, we would expect a larger fraction of high-stretch SNe, which are associated with higher R_V values. Moreover, high-stretch SNe are typically found in more star-forming galaxies, while low-stretch SNe are predominantly located in quiescent hosts, paralleling the R_V trend observed by Salim et al. (2018). Together, these results might suggest that the two main hypotheses proposed to explain the origin of the mass step may, in fact, share a common physical origin: two different progenitor channels associated to different environments.

6. Conclusions

In this work, we examine how improving the match between the SNe light curve parameters c and x_1 , and the corresponding host properties $\log(M/M_\odot)$ and $\log(\text{sSFRyr})$ distributions in subsamples drawn from the calibration and Hubble Flow SNe samples used in the Riess et al. (2022) analysis affects the SN luminosity standardization, as well as the Hubble constant H_0 estimation. Using a full sample of 253 SNe, our main findings are as follows.

(i) The calibration sample is not fully representative of the Hubble Flow sample according to K-S test results, in terms of the stellar mass (p -value = 5.067×10^{-4}) and the specific star formation rate (p -value = 3.029×10^{-2}), as shown in Section 4.1. There is a clear difference between the $\log(M/M_\odot)$ distributions of the two samples, with the calibration sample containing SNe hosted in more massive galaxies than those found in the HF sample. Regarding $\log(\text{sSFRyr})$, the calibration sample includes SNe in galaxies with much higher sSFR values that are not present in the HF sample, while the latter shows lower values that are not seen in the SN calibration sample (see Figures 1 and 2).

(ii) A subsample from the HF capable of independently resolving the Hubble tension may not exist, regardless of its agreement with the entire calibration sample or the specific properties considered. In order to achieve a more accurate SN luminosity correction and potentially reduce the Hubble tension, intrinsic

discrepancies in the property distributions must be addressed in both the HF and calibration samples.

(iii) We find statistical significant linear relations between the H_0 (6.84σ), M_B (9.31σ), α (3.78σ) and σ_{int} (6.00σ) and the improved matching of the property distributions between the randomly generated calibration and HF subsamples, even though this relations do not strongly change any of the standardization parameters, nor the value of H_0 , as shown in Table 2.

(iv) Although the possible effects of subsample sizes (section 5.3) and the choice of mass threshold used to define the mass step may influence the relationship between the improved matching of subsample properties and the estimated Δ_{host} and corresponding uncertainties, our results indicate that more consistent subsamples tend to produce a mass step consistent with zero within 1σ uncertainty, as shown in Figure 5.

(v) We find notable discrepancies between the estimated values of H_0 ($2.00 - 3.30 \sigma$) and M_B ($1.74 - 2.90 \sigma$) when comparing different subpopulations of SN characterized by their x_1 . The higher-stretch subpopulation yields consistently lower values of both H_0 and M_B compared to the lower-stretch one, regardless of the method used to define the SN subpopulations (see Tables 5, 10, 13, 15). These differences in the estimated H_0 and M_B between low- and high-stretch SNe are likely due to the absence of additional bias correction terms and the simplified β -colour correction, which assumes that extinction and intrinsic colour effects are indistinguishable and identical for all SNe. However, these assumptions do not seem to be accurate, as inconsistencies in R_V between the calibration and Hubble flow samples within the low-stretch bin, which are not fully accounted for by the β colour term, appear to be the cause of the higher H_0 and M_B values (see Figure 10). This inconsistency may arise from the natural selection of late-type, star-forming host galaxies for Cepheid observations, which can result in a calibration sample predominantly composed of high-stretch SNe, as suggested by Wojtak, R. & Hjorth, J. (2025). The differing behavior between the two stretch populations, not only in the inferred values of H_0 and M_B but also in their response to changes in the β parameter, points to clear intrinsic and/or dust differences between the populations.

(vi) Our findings suggest that the H_0 and M_B uncertainties commonly reported in the literature may themselves be underestimated, as they do not account for the additional dispersion effect in both parameters distributions arising from different underlying SN subpopulations, as clearly illustrated in Figure 11. Considering the lower uncertainty obtained when treating the subpopulations independently as the true uncertainty of the full SN sample H_0 estimate (Table 1), we obtain $H_0 = 73.781 \pm 2.166 \text{ km s}^{-1} \text{ Mpc}^{-1}$. Under this assumption, the tension with the Planck Collaboration et al. (2020) measurement would decrease from approximately 5.87σ to about 2.53σ (see Figure 12).

(vii) The mass step seems to be consistent with 0 for both stretch subpopulations (see Tables 6, 11, 14, 16 and Figure 8). This result, allied to the different M_B and underlying R_V found for both SN subpopulations, suggests that this effect may arise from an over-correction of more than one subpopulation with different properties occurring in different environments, in an attempt to account for their intrinsic absolute magnitude and total-to-selective coefficients rather than treating the subpopulations separately, as suggested in Section 5.4.

To conclude, we place into perspective the tension between the late-time measurements of H_0 obtained in this work and the early-time estimate of $H_0 = 67.4 \pm 0.5 \text{ km s}^{-1} \text{ Mpc}^{-1}$ from Planck Collaboration et al. (2020), as shown in Figure 12, alongside the tension between the latter and the late-time measurement of $H_0 = 73.04 \pm 1.04 \text{ km s}^{-1} \text{ Mpc}^{-1}$ reported by Riess

et al. (2022). In this work, we find $H_0 = 71.25 \pm 1.59 \text{ km s}^{-1} \text{ Mpc}^{-1}$ using SNe from the high-stretch bin (presumably representing the younger SN subpopulation), and $H_0 = 75.27 \pm 1.18 \text{ km s}^{-1} \text{ Mpc}^{-1}$ using SNe from the low-stretch bin (presumably representing the older SN subpopulation). We can see a reduction of the tension between the late-time and early-time measurements in Figure 12, when only using SNe from the bin with higher stretch (2.52σ) in relation to the value estimated using all the SNe from the full sample (4.81σ ; Riess et al. 2022). From this Figure and also comparing all the results from our work, it even seems that the full sample H_0 and M_B estimations might result from the simultaneous contribution of the underlying old and younger SNe subpopulations characterized by a lower and higher values of x_1 respectively. Our estimation of $H_0 = 73.78 \pm 2.17 \text{ km s}^{-1} \text{ Mpc}^{-1}$ obtained using the full sample of SNe and accounting for uncertainties by treating the two subpopulations of stretch independently is also shown in Figure 12, reducing the tension to a discrepancy of 2.86σ .

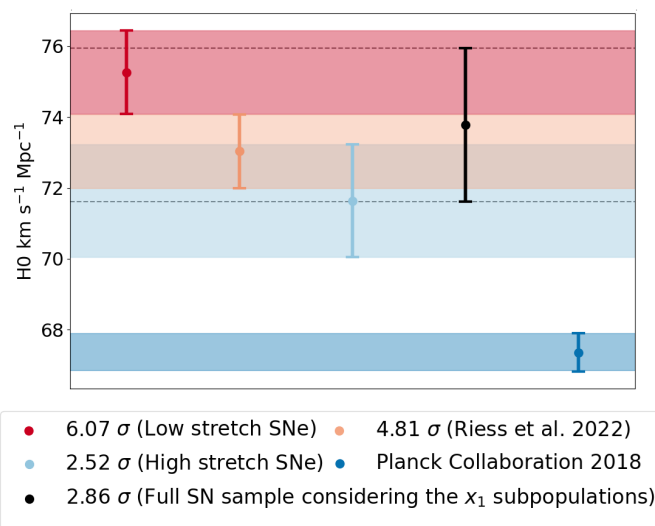


Fig. 12: The Figure displays the H_0 estimates and their associated uncertainties obtained in this work using the high-stretch (light blue) and low-stretch (red) SNe bins, alongside the measurement from Riess et al. (2022) (orange) and the early-time estimate from Planck Collaboration et al. (2020) (dark blue). The H_0 obtained in this work using the full sample of SNe and accounting for uncertainties by treating the two subpopulations of stretch independently (black) is also shown. All significance values reported in the legend correspond to the level of discrepancy between each late-time measurement of H_0 and the early-time value of the Hubble parameter (in blue).

Our study can be improved in several aspects, mainly in the modeling and distinction of the SNe mixed subpopulations. For future work, we aim to distinguish the two SN Ia subpopulations in a more rigorous manner by applying other clustering algorithms, such as the HDBSCAN (McInnes et al. 2017). We would also like to incorporate other host galaxy properties such as their morphology (e.g., Baluta et al. 2024; Suzuki et al. 2012) and use local properties, as type Ia supernova luminosities appear to correlate more strongly with local rather than global host properties (e.g., Kim et al. 2018; Rose et al. 2019; Rigault et al. 2020b). Moreover, increasing the amount of data would be very useful to identify stronger and more significant relationships between SN luminosities and their environmental properties. It would also al-

low for a clearer separation of different SN subpopulations, particularly within the calibration sample, where the current number of SNe is still limited. Future analyses could also incorporate the volume-limited Zwicky Transient Facility (ZTF) SN Ia DR2 dataset (Rigault et al. 2025), as well as SN Ia light-curve data compiled by the Carnegie Supernova Project (CSP) I and II (Krisenciunas et al. 2017; Phillips et al. 2019) and the upcoming data from the Vera Rubin Observatory's Legacy Survey of Space and Time (LSST; Ivezić et al. 2019).

Acknowledgements. G. M., J. D., and A. M. acknowledge support by FCT for CENTRA through the Project No. UID/99/2025. J. D. also acknowledges support by FCT under the PhD grant 2023.01333.BD, with DOI <https://doi.org/10.54499/2023.01333.BD>. S.G.G. acknowledges support from the ESO Scientific Visitor Programme. All authors thank Rita Santos for her insightful comments and suggestions on the work.

References

Abbott, B. P. et al. 2017, *Nature*, 551, 85–88

Anderson, R. I. 2024, in *The Hubble Constant Tension* (Springer), 89–119

Baluta, A. Y. et al. 2024, *Communications of the Byurakan Astrophysical Observatory*, 316–320

Betoule, M. et al. 2014, *Astronomy & Astrophysics*, 568, A22

Birrer, S. et al. 2024, *Time-Delay Cosmography: Measuring the Hubble Constant and other cosmological parameters with strong gravitational lensing*

Branch, D. & Tammann, G. 1992, In: *Annual review of astronomy and astrophysics*, Vol. 30 (A93-25826 09-90), p. 359–389., 30, 359

Brandt, T. D. et al. 2010, *The Astronomical Journal*, 140, 804–816

Brout, D. & Scolnic, D. 2021, *The Astrophysical Journal*, 909, 26

Brout, D. et al. 2022, *The Astrophysical Journal*, 938, 110

Camarena, D. & Marra, V. 2021, *Monthly Notices of the Royal Astronomical Society*, 504, 5164–5171

Childress, M. J. et al. 2014, *Monthly Notices of the Royal Astronomical Society*, 445, 1898

Chow, I. & Brown, P. G. 2025, *Icarus*, 429, 116444

Chung, C. et al. 2023, *The Astrophysical Journal*, 959, 94

Chung, C. et al. 2025, *Strong progenitor age bias in supernova cosmology. I. Robust and ubiquitous evidence from a larger sample of host galaxies in a broader redshift range*

Conley, A. et al. 2007, *The Astrophysical Journal*, 664, L13

De Jaeger, T., Stahl, B., Zheng, W., et al. 2020, *Monthly Notices of the Royal Astronomical Society*, 496, 3402

Dempster, A. P. et al. 1977, *Journal of the Royal Statistical Society. Series B (Methodological)*, 39, 1

Dhawan, S., Jha, S. W., & Leibundgut, B. 2018, *Astronomy & Astrophysics*, 609, A72

Duarte, J. et al. 2023, *Astronomy & Astrophysics*, 680, A56

Fasano, G. & Franceschini, A. 1987, *Monthly Notices of the Royal Astronomical Society*, 225, 155

Feldmann, R. 2017, *Monthly Notices of the Royal Astronomical Society: Letters*, 470, L59

Fisher, R. A. 1935, *The Design of Experiments* (Edinburgh: Oliver and Boyd)

Fitzpatrick, E. L. & Massa, D. 2007, *The Astrophysical Journal*, 663, 320

Foreman-Mackey, D. et al. 2013, *PASP*, 125, 306

Freedman, W. L. & Madore, B. F. 2010, *Annual Review of Astronomy and Astrophysics*, 48, 673–710

Freedman, W. L. et al. 2019, *The Astrophysical Journal*, 882, 34

Garnavich, P. et al. 2023, *The Astrophysical Journal*, 953, 35

Ginolini, M. et al. 2025, *Astronomy & Astrophysics*, 695, A140

González-Gaitán, S. et al. 2021, *Monthly Notices of the Royal Astronomical Society*, 508, 4656–4666

Groenewegen, M. A. T. 2018, *Astronomy & Astrophysics*, 619, A8

Guy, J. et al. 2010, *Astronomy & Astrophysics*, 523, A7

Hahn, C. et al. 2019, *The Astrophysical Journal*, 872, 160

Hoyle, F. & Fowler, W. A. 1960, *ApJ*, 132, 565

Hu, J.-P. & Wang, F.-Y. 2023, *Universe*, 9, 94

Huang, C. D. et al. 2020, *The Astrophysical Journal*, 889, 5

Ivezić, Ž., Kahn, S. M., Tyson, J. A., et al. 2019, *The Astrophysical Journal*, 873, 111

Johansson, J. et al. 2021, *The Astrophysical Journal*, 923, 237

Jönsson, J. et al. 2010, *Monthly Notices of the Royal Astronomical Society*, 405, 535

Kang, Y. et al. 2016, *The Astrophysical Journal Supplement Series*, 223, 7

Kang, Y. et al. 2020, *The Astrophysical Journal*, 889, 8

Kasa, S. R. & Rajan, V. 2023, *Scientific Reports*, 13, 19164

Kelly, P. L. et al. 2010, *The Astrophysical Journal*, 715, 743
 Kelly, P. L. et al. 2015, *Science*, 347, 1459
 Kelsey, L. et al. 2022, *Monthly Notices of the Royal Astronomical Society*, 519, 3046–3063
 Kessler, R. & Scolnic, D. 2017, *The Astrophysical Journal*, 836, 56
 Khetan, N. et al. 2021, *Astronomy & Astrophysics*, 647, A72
 Kim, Y.-L. et al. 2018, *The Astrophysical Journal*, 854, 24
 Kolmogorov, 1933, *Giorn Dell'inst Ital Degli Att*, 4, 89
 Krisciunas, K. et al. 2017, *Astronomical Journal*, 154, 211
 Larison, C. et al. 2024, *The Astrophysical Journal*, 961, 185
 Leavitt, H. S. 1908, *Annals of Harvard College Observatory*, vol. 60, pp. 87–108.3, 60, 87
 Lee, Y.-W., Chung, C., Kang, Y., & Jee, M. J. 2020, *The Astrophysical Journal*, 903, 22
 Lee, Y.-W. et al. 2022, *Monthly Notices of the Royal Astronomical Society*, 517, 2697
 Marquardt, D. W. 1970, *Technometrics*, 12, 591
 McInnes, L. et al. 2017, *J. Open Source Softw.*, 2, 205
 McLachlan, G. J. & Peel, D. 2000, *Finite mixture models* (John Wiley & Sons)
 Monge, G. 1784, *Mémoire sur le calcul intégral des équations aux différences partielles* (Imprimerie royale)
 Murakami, Y. S. & Scolnic, D. 2025, Reassessing the ZTF Volume-Limited Type Ia Supernova Sample and Its Implications for Continuous, Dust-Dependent Models of Intrinsic Scatter
 Neill, J. D. et al. 2009, *The Astrophysical Journal*, 707, 1449–1465
 Nicolas, N. et al. 2021, *Astronomy & Astrophysics*, 649, A74
 Pan, Y.-C. 2020, *The Astrophysical Journal Letters*, 895, L5
 Panaretos, V. M. & Zemel, Y. 2019, *Annual review of statistics and its application*, 6, 405
 Pedregosa, F. et al. 2011, *Journal of Machine Learning Research*, 12, 2825
 Peebles, P. J. E. 1984, *Astrophys. J.*, 284, 439
 Peebles, P. J. E. 2020, *Principles of Physical Cosmology* (Princeton University Press)
 Petersen, K. & Pedersen, M. 2006, *The Matrix Cookbook* (Technical University of Denmark), version 20121115
 Phillips, M. M. 1993, *Astrophysical Journal, Part 2-Letters (ISSN 0004-637X)*, vol. 413, no. 2, p. L105-L108., 413, L105
 Phillips, M. M. et al. 2019, *Publications of the Astronomical Society of the Pacific*, 131, 014001
 Pitman, E. J. 1937, *Supplement to the Journal of the Royal Statistical Society*, 4, 119
 Planck Collaboration et al. 2020, *Astronomy & Astrophysics*, 641, A6
 Ponder, K. A. et al. 2021, *The Astrophysical Journal*, 923, 197
 Popovic, B. et al. 2023, *The Astrophysical Journal*, 945, 84
 Prughinskaya, M. V. et al. 2020, *Monthly Notices of the Royal Astronomical Society*, 499, 5121
 Ramirez, M. et al. 2024, *Astronomy & Astrophysics*, 691, A33
 Riess, A. G. et al. 2016, *The Astrophysical Journal*, 826, 56
 Riess, A. G. et al. 2022, *The Astrophysical Journal Letters*, 934, L7
 Rigault, M. et al. 2013, *Astronomy & Astrophysics*, 560, A66
 Rigault, M. et al. 2015, *The Astrophysical Journal*, 802, 20
 Rigault, M. et al. 2020a, *Astronomy & Astrophysics*, 644, A176
 Rigault, M. et al. 2020b, *Astronomy & Astrophysics*, 644, A176
 Rigault, M. et al. 2025, *Astronomy & Astrophysics*, 694, A2
 Rizzo, M. L. & Székely, G. J. 2016, *wiley interdisciplinary reviews: Computational statistics*, 8, 27
 Rose, B. M. et al. 2019, *The Astrophysical Journal*, 874, 32
 Rousseeuw, P. J. 1987, *Journal of Computational and Applied Mathematics*, 20, 53
 Salim, S. et al. 2018, *The Astrophysical Journal*, 859, 11
 Schlafly, E. F. et al. 2016, *The Astrophysical Journal*, 821, 78
 Scolnic, D. et al. 2022, *The Astrophysical Journal*, 938, 113
 Smirnov, N. V. 1939, *Bull. Math. Univ. Moscou*, 2, 3
 Steinhardt, C. L. et al. 2020, *The Astrophysical Journal*, 902, 14
 Steinhaus, H. et al. 1956, *Bull. Acad. Polon. Sci.*, 1, 801
 Sullivan, M. et al. 2010, *Monthly Notices of the Royal Astronomical Society*, 406, 782
 Suzuki, N. et al. 2012, *The Astrophysical Journal*, 746, 85
 Thorp, S. & Mandel, K. S. 2022, *Monthly Notices of the Royal Astronomical Society*, 517, 2360
 Toy, M. et al. 2025, *Monthly Notices of the Royal Astronomical Society*, 538, 181
 Tripp, R. 1998, *Astronomy and Astrophysics*, v. 331, p. 815–820 (1998), 331, 815
 Uddin, S. A. et al. 2017, *The Astrophysical Journal*, 848, 56
 Uddin, S. A. et al. 2020, *The Astrophysical Journal*, 901, 143
 Valentino, D. et al. 2021, *Classical and Quantum Gravity*, 38, 153001
 Virtanen, P. et al. 2020, *Nature Methods*, 17, 261
 Visser, M. 2004, *Classical and Quantum Gravity*, 21, 2603
 Vogl, C., Taubenberger, S., Csörnyei, G., et al. 2025, *A&A*, 702, A41
 Wang, X., Wang, L., Filippenko, A. V., Zhang, T., & Zhao, X. 2013, *Science*, 340, 170
 Wiseman, P. et al. 2023a, *Monthly Notices of the Royal Astronomical Society*, 520, 6214
 Wiseman, P. et al. 2023b, *Monthly Notices of the Royal Astronomical Society*, 520, 6214
 Wojtak, R. & Hjorth, J. 2022, *Monthly Notices of the Royal Astronomical Society*, 515, 2790–2799
 Wojtak, R. & Hjorth, J. 2024, Consistent extinction model for type Ia supernovae in Cepheid-based calibration galaxies and its impact on H_0
 Wojtak, R. et al. 2023, *Monthly Notices of the Royal Astronomical Society*, 525, 5187
 Wojtak, R. & Hjorth, J. 2025, *Astronomy & Astrophysics*, 702, A176

A. Results from the property binning analysis

A.1. Dividing the bins by the median property value

SNe bin	Number of SNe	H_0	Sig.	M_B	Sig.	α	Sig.
$c < \tilde{c}$	126	$72.937^{+1.217}_{-1.224}$	1.11 σ	$-19.204^{+0.038}_{-0.040}$	0.12 σ	$0.127^{+0.013}_{-0.013}$	0.52 σ
$c \geq \tilde{c}$	127	$75.045^{+1.463}_{-1.456}$		$-19.198^{+0.040}_{-0.041}$		$0.137^{+0.017}_{-0.016}$	
$x_1 < \tilde{x}_1$	126	$75.266^{+1.191}_{-1.166}$	2.00 σ	$-19.155^{+0.033}_{-0.033}$	2.23 σ	$0.128^{+0.022}_{-0.023}$	0.42 σ
$x_1 \geq \tilde{x}_1$	127	$71.247^{+1.638}_{-1.546}$		$-19.293^{+0.052}_{-0.051}$		$0.112^{+0.029}_{-0.030}$	
$\log(M/M_\odot) < \log(\tilde{M}/M_\odot)$	126	$72.627^{+1.634}_{-1.638}$	1.05 σ	$-19.210^{+0.047}_{-0.049}$	0.21 σ	$0.134^{+0.016}_{-0.016}$	0.31 σ
$\log(M/M_\odot) \geq \log(\tilde{M}/M_\odot)$	127	$74.711^{+1.160}_{-1.142}$		$-19.198^{+0.031}_{-0.031}$		$0.141^{+0.014}_{-0.014}$	
$\log(\text{sSFRyr}) < \log(\tilde{\text{sSFRyr}})$	123	$74.702^{+1.332}_{-1.193}$	1.13 σ	$-19.182^{+0.036}_{-0.034}$	0.84 σ	$0.136^{+0.013}_{-0.013}$	0.35 σ
$\log(\text{sSFRyr}) \geq \log(\tilde{\text{sSFRyr}})$	130	$72.526^{+1.513}_{-1.434}$		$-19.228^{+0.042}_{-0.042}$		$0.129^{+0.017}_{-0.017}$	

Table 5: Estimated H_0 , M_B and α using SNe from two different bins divided by the median value for each property c , x_1 , $\log(M/M_\odot)$, and $\log(\text{sSFRyr})$ distribution of the full sample and their respective difference to the 16th and 84th percentiles. The significances of the differences between the estimated parameters for each bin of the considered property (Sig.) are also shown.

SNe bin	Number of SNe	β	Sig.	Δ_{host}	Sig.	σ_{int}	Sig.
$c < \tilde{c}$	126	$2.837^{+0.241}_{-0.235}$	1.10 σ	$-0.020^{+0.010}_{-0.011}$	0.39 σ	$0.073^{+0.015}_{-0.017}$	0.72 σ
$c \geq \tilde{c}$	127	$3.220^{+0.258}_{-0.252}$		$-0.013^{+0.014}_{-0.014}$		$0.090^{+0.016}_{-0.016}$	
$x_1 < \tilde{x}_1$	126	$2.861^{+0.144}_{-0.147}$	0.94 σ	$-0.016^{+0.012}_{-0.012}$	0.23 σ	$0.083^{+0.013}_{-0.013}$	0.92 σ
$x_1 \geq \tilde{x}_1$	127	$2.633^{+0.192}_{-0.193}$		$-0.012^{+0.012}_{-0.012}$		$0.100^{+0.013}_{-0.013}$	
$\log(M/M_\odot) < \log(\tilde{M}/M_\odot)$	126	$2.910^{+0.178}_{-0.170}$	0.75 σ	$-0.017^{+0.012}_{-0.012}$	0.18 σ	$0.079^{+0.015}_{-0.016}$	0.68 σ
$\log(M/M_\odot) \geq \log(\tilde{M}/M_\odot)$	127	$2.736^{+0.159}_{-0.155}$		$-0.020^{+0.012}_{-0.012}$		$0.092^{+0.013}_{-0.012}$	
$\log(\text{sSFRyr}) < \log(\tilde{\text{sSFRyr}})$	123	$2.751^{+0.158}_{-0.163}$	0.16 σ	$-0.024^{+0.012}_{-0.012}$	0.90 σ	$0.089^{+0.013}_{-0.012}$	0.22 σ
$\log(\text{sSFRyr}) \geq \log(\tilde{\text{sSFRyr}})$	130	$2.787^{+0.180}_{-0.163}$		$-0.008^{+0.013}_{-0.013}$		$0.093^{+0.014}_{-0.013}$	

Table 6: Same as Table 5 for the remaining parameters β , Δ_{host} and σ_{int} .

A.2. Using subsamples from the high and low stretch bins defined with \tilde{x}_1

SNe bin	H_0	Sig.	M_B	Sig.	α	Sig.
$x_1 < \tilde{x}_1$	$75.315^{+0.877}_{-0.859}$	3.30 σ	$-19.156^{+0.022}_{-0.025}$	2.90 σ	$0.129^{+0.021}_{-0.025}$	0.21 σ
$x_1 \geq \tilde{x}_1$	$71.640^{+0.710}_{-0.774}$		$-19.276^{+0.033}_{-0.030}$		$0.118^{+0.046}_{-0.037}$	

Table 7: Estimated median values of H_0 , M_B , and α , with differences relative to the 16th and 84th percentiles, for SNe subsamples drawn from the two stretch bins defined by \tilde{x}_1 . The significances of the differences between the estimated parameters for each bin (Sig.) are also shown.

SNe bin	β	Sig.	Δ_{host}	Sig.	σ_{int}	Sig.
$x_1 < \tilde{x}_1$	$2.901^{+0.174}_{-0.116}$	0.91σ	$-0.015^{+0.013}_{-0.013}$	0σ	$0.078^{+0.012}_{-0.019}$	0.36σ
$x_1 \geq \tilde{x}_1$	$2.633^{+0.269}_{-0.293}$		$-0.015^{+0.014}_{-0.014}$		$0.089^{+0.025}_{-0.029}$	

Table 8: Same as Table 7 for β , Δ_{host} and σ_{int} .

B. Minimizing the subpopulations mixing

For the stretch parameter, Wojtak et al. (2023) identify distinct, though overlapping, SN populations that can be primarily distinguished by their mean stretch values, obtained by fitting a bimodal Gaussian distribution. Using the Pantheon+ light-curve parameters (Brout et al. 2022), they find mean values of $\bar{x}_1 \approx -1.22$ and $\bar{x}_1 \approx 0.42$ for the two subpopulations. In our sample, the mean values for each bin defined by stretch are higher, with the low-stretch bin yielding a value of $\bar{x}_1 \approx -0.45$ and the high-stretch bin a value of $\bar{x}_1 \approx 0.74$. In Ginolini et al. (2025), the authors employ a broken- α standardization model aimed at reducing Hubble residuals. In this work, they fit the break point separating the two x_1 modes and obtain a value of $x_1 = -0.48$, significantly lower than the one we use to separate our bins ($x_1 = 0.087$). Additionally, they also fit a bimodal Gaussian distribution to the stretch parameter, finding mean values of $\bar{x}_1 \approx 0.42$ for the high-stretch mode and $\bar{x}_1 \approx -1.24$ for the low-stretch mode.

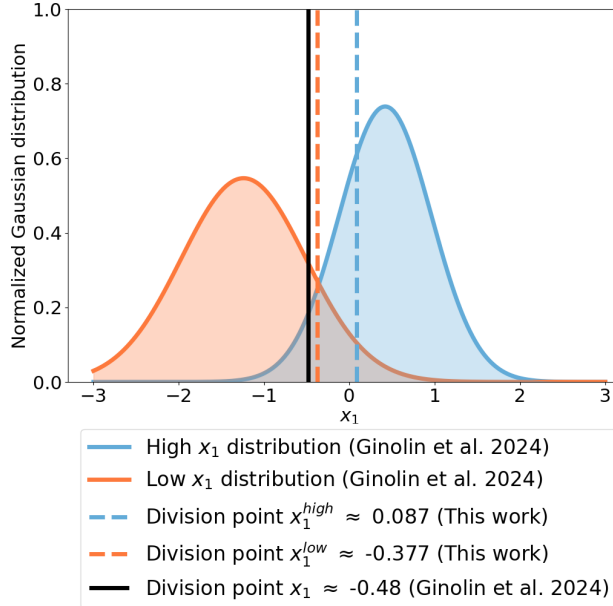


Fig. 13: Normalized Gaussian distributions representing the high-stretch (blue) and low-stretch (orange) SN populations, using the fitted parameters from Ginolini et al. (2025). The vertical solid line indicates the x_1 break point between the two stretch modes obtained in the cited study, while the vertical dashed lines mark the splitting points adopted in this study to reduce the overlap of the two SN subpopulations. The shaded region highlights the overlap between the two distributions.

As we can see in Figure 13, by choosing a higher x_1 splitting value ($\tilde{x}_1 = 0.087$ in our case), as opposed to the lower thresholds used in the literature (e.g., $x_1 = -1$ in Garnavich et al. (2023) and Larison et al. (2024), or $x_1 \approx -0.5$ in Ginolini et al. (2025)), we are guaranteeing that our higher stretch bin is mainly assessing the higher-stretch SN population, typ-

ically associated with younger progenitors (e.g., Nicolas et al. 2021). This choice reduces the risk of contamination from the low-stretch mode, typically associated to older progenitors, in our high-stretch bin. In contrast, the defined lower stretch bin in our study may include an overlap between the two subpopulations, especially in the x_1 range between approximately -1 and 0. While this overlap may have only a modest impact, it might not be negligible. To mitigate this contamination, one possible alternative would be to adopt a three-bin strategy, as in Kelly et al. (2010), where the authors divide the stretch parameter into $x_1 < -1$, $-1 < x_1 < 0$, and $x_1 > 0$. This method allows a cleaner separation between the two populations, particularly in the overlapping region. However, this can reduce the statistical precision of the estimated parameters for each bin due to the limited number of calibrators. Instead, we redefine the bins by selecting SNe below the 30th percentile ($x_1^{\text{low}} = -0.377$) and above the median ($x_1^{\text{high}} = 0.087$) of the stretch distribution, as also presented in the Figure. Although this approach does not completely exclude the overlapping region, it reduces the number of SNe that may be misclassified between the high- and low-stretch bins while maintaining sufficient calibrators in both cases.

Overall, the results remain consistent with those obtained using the median stretch x_1 value ($\bar{x}_1 = 0.087$) as a division point of the stretch distribution. The most notable differences are again found for H_0 and M_B , as shown in Table 10, although the discrepancy in the latter has decreased compared to the median-based division (see Table 3), with differences of 2.00σ and 1.75σ , respectively. This reduction may partly result from the smaller number of SNe included in the low-stretch bin, while the number of SNe in the high-stretch bin remains unchanged for the two approaches. Again, no other notable variations are found for the remaining parameters estimated from the two different stretch bins and the mass step is nearly consistent with 0 within 1σ uncertainties for both bins, obtaining $\Delta_{\text{host}} = -0.012 \pm 0.017$ (0.71σ) for the low-stretch bin and $\Delta_{\text{host}} = -0.013 \pm 0.012$ (1.08σ) for the high-stretch bin. A complete summary of all parameters estimated using this approach, along with the corresponding discrepancies, is provided in Tables 10 and 11.

C. Accessing SN subpopulations using other approaches

C.1. Maximizing the property distributions matching

As a way of trying to obtain a more accurate threshold for dividing the stretch distribution and distinguishing the two SN subpopulations, we estimated the value of x_1 that, when used as a division point in the full stretch distribution, maximizes the agreement between the calibration and Hubble flow distributions across all properties for the two stretch populations, hereafter denoted as x_1^* . To do that, and taking into account the division points between stretch modes reported in previous studies such as $x_1 = -1$ for Larison et al. (2024) and $x_1 = -0.48$ for Ginolini et al. (2025), we defined an interval for x_1^* ranging from -1.5 to 0.5 in steps of 0.001. For each candidate threshold, we performed K-S tests comparing the distributions of c , $\log(M/M_\odot)$,

SNe bin	Number of SNe	H_0	Sig.	M_B	Sig.	α	Sig.
$x_1 < x_1^{\text{low}}$	76	$75.863^{+1.687}_{-1.875}$		$-19.169^{+0.051}_{-0.050}$		$0.149^{+0.037}_{-0.037}$	
$x_1 \geq x_1^{\text{high}}$	127	$71.249^{+1.576}_{-1.567}$	2.00σ	$-19.291^{+0.049}_{-0.052}$	1.74σ	$0.113^{+0.029}_{-0.028}$	0.77σ

Table 10: Estimated H_0 , M_B and α using SNe from two different stretch bins. The low-stretch bin includes SNe with x_1 below $x_1^{\text{low}} = -0.377$, while the high-stretch bin includes SNe with x_1 above the $x_1^{\text{high}} = 0.087$ threshold. The significances of the differences between the estimated parameters for each bin (Sig.) are also shown.

SNe bin	Number of SNe	β	Sig.	Δ_{host}	Sig.	σ_{int}	Sig.
$x_1 < x_1^{\text{low}}$	76	$2.829^{+0.185}_{-0.178}$		$-0.012^{+0.017}_{-0.017}$		$0.096^{+0.017}_{-0.016}$	
$x_1 \geq x_1^{\text{high}}$	127	$2.626^{+0.194}_{-0.193}$	0.77σ	$-0.013^{+0.012}_{-0.012}$	0.05σ	$0.101^{+0.013}_{-0.013}$	0.23σ

Table 11: Same as Table 10 for the remaining parameters β , Δ_{host} and σ_{int} .

and $\log(\text{sSFRyr})$ between the calibration and Hubble flow samples within each bin divided by x_1^* . The final value of x_1^* was chosen as the one that maximized the resulting product of all the estimated p -values.

We obtained a value of $x_1^* = -0.334$, which produced a notable improvement in the agreement between the calibration and Hubble flow samples for the $\log(M/M_\odot)$ distribution in the lower-stretch bin and for the $\log(\text{sSFRyr})$ distribution in the higher-stretch bin, relative to the values obtained using the median value of $\tilde{x}_1 = 0.087$ as a division threshold, as shown in Table 12. On the other hand, adopting this improved threshold also led to a significant decrease in the agreement of the stretch distributions within the lower-stretch bin.

As expected, the p -values for the lower-stretch bin upper limited by $x_1^{\text{low}} = -0.377$ are very similar to those obtained using x_1^* , given the close proximity of the division values, which results in nearly identical SNe composing both bins and thus similar property distributions. Conversely, the p -values for the higher-stretch bin lower limited by $x_1^{\text{high}} = 0.087$ are equal to those derived using \tilde{x}_1 . This reproduces the previously observed increase in the p -values for the $\log(\text{sSFRyr})$ distributions in the high-stretch bin when the division point is changed from \tilde{x}_1 to x_1^* , as well as the observed decrease in the p -value for the x_1 parameter in the lower-stretch bin. All other properties exhibit consistent p -values across the bins defined by the different division points with only the $\log(M/M_\odot)$ distribution in the higher-stretch bin, yielding p -values below the significance threshold of 0.05 for both cases.

Comparing the values of H_0 , M_B , α , and β estimated using all SNe from the two bins defined by x_1^* , presented in Tables 13 and 14, we find results broadly consistent with those obtained when using either the median of the full stretch distribution or the 40th and 50th percentiles of the full SN sample stretch distribution as division thresholds, with the largest discrepancies being found for the H_0 and M_B estimated from the different bins. However, except for the H_0 case, all the discrepancies seem to be less significant when using the x_1^* as the division value to separate the high and low stretch modes bins. We also note that both H_0 and α take slightly higher values under this separation. These differences may result from the lower division value of x_1^* compared to the division values defined across Section 4.5, which, while reducing the potential misclassification of SNe from the higher-stretch subpopulation into the lower-stretch bin, can increase the overlap between the two subpopulations within the defined high-stretch bin, as shown in Figure 13. This behavior

is similar to what we observed for the SN bins obtained by dividing the stretch distribution using \tilde{x}_1 , although in that case the subpopulation mixing primarily affects the lower-stretch bin. In contrast, the effect on the estimated H_0 and α is the opposite, as the parameters are lower in both stretch bins.

C.2. Applying Gaussian Mixture Models

The Gaussian Mixture Model (GMM) is a probabilistic method that assumes that the data is generated from a mixture of several Gaussian distributions with unknown parameters, each corresponding to a distinct cluster (McLachlan & Peel 2000). Typically, the algorithm begins by initializing the means, covariances, and weights of the Gaussian distributions, often using k-means clustering for preliminary labeling (Steinhaus et al. 1956), and then iteratively refines these parameters by fitting the GMM to the data with the Expectation-Maximization (EM) algorithm (Dempster et al. 1977). One of the main limitations of Gaussian Mixture clustering is that the number of clusters must be specified in advance. In our case, however, this is not a critical drawback, since we aim to identify and distinguish the two already documented SN subpopulations characterized by their stretch distribution and strong host environment dependence (e.g., Nicolas et al. 2021; Ginolini et al. 2025), which naturally motivates the choice of two clusters.

To evaluate and compare the quality of the clustering results, we computed the Silhouette score (Rousseeuw 1987) for each group of clusters, which quantifies how well each data point fits within its assigned cluster and how clearly it is separated from other clusters. Both the GMM algorithm and the Silhouette score were implemented using the *scikit-learn* python package (Pedregosa et al. 2011). We applied the GMM clustering algorithm to different combinations of c , x_1 , $\log(M/M_\odot)$, and $\log(\text{sSFRyr})$ distributions in an attempt to distinguish the different SN subpopulations. Besides all possible combinations of lightcurve and host properties, meaningful and scientifically motivated clustering was only obtained when applying GMM clustering to the x_1 and $\log(M/M_\odot)$ distributions together, obtaining the clusters whose density contours are presented in Figure 14.

We then proceed to estimate the cosmological parameters for each cluster, along with the standardization parameters listed in Tables 15 and 16. The largest discrepancies arise in the estimated H_0 and β between the lower and higher stretch SN clusters, with significances of 1.23σ and 1.22σ respectively. All parameters appear consistent with the results and conclusions of the pre-

Division value	Lower stretch bin				Higher stretch bin			
	c	x_1	$\log(M/M_\odot)$	$\log(\text{sSFRyr})$	c	x_1	$\log(M/M_\odot)$	$\log(\text{sSFRyr})$
\tilde{x}_1	0.986	0.763	0.007	0.259	0.417	0.198	0.048	0.094
$x_1^{\text{low/high}}$	0.733	0.305	0.056	0.252	0.417	0.198	0.048	0.094
x_1^*	0.982	0.187	0.062	0.298	0.534	0.212	0.037	0.336

Table 12: Estimated p -values comparing the calibration and Hubble Flow sample property distributions across different stretch binning thresholds: the median of the full sample ($\tilde{x}_1 = 0.087$), the 30th ($x_1^{\text{low}} = -0.377$) and 50th percentiles ($x_1^{\text{high}} = 0.087$) of the x_1 distribution, and the value that maximizes the overall agreement between the calibration and Hubble Flow samples ($x_1^* = -0.334$).

SNe bin	Number of SNe	H_0	Sig.	M_B	Sig.	α	Sig.
$x_1 < x_1^*$	80	$76.386^{+1.602}_{-1.548}$	2.30σ	$-19.162^{+0.045}_{-0.046}$	1.42σ	$0.153^{+0.034}_{-0.034}$	0.34σ
$x_1 > x_1^*$	173	$71.794^{+1.250}_{-1.240}$		$-19.246^{+0.037}_{-0.037}$		$0.140^{+0.018}_{-0.018}$	

Table 13: Estimated H_0 , M_B , α and β using SNe from two different bins divided by $x_1^* = -0.334$ and their respective difference to the 16th and 84th percentiles. The significance of the differences between the estimated parameters for each bin of the considered property (Sig.) are also shown.

SNe bin	Number of SNe	β	Sig.	Δ_{host}	Sig.	σ_{int}	Sig.
$x_1 < x_1^*$	80	$2.849^{+0.169}_{-0.168}$	0.21σ	$-0.014^{+0.016}_{-0.015}$	0.32σ	$0.092^{+0.017}_{-0.016}$	0.15σ
$x_1 > x_1^*$	173	$2.801^{+0.150}_{-0.152}$		$-0.008^{+0.010}_{-0.010}$		$0.089^{+0.012}_{-0.011}$	

Table 14: Same as Table 13 for the remaining parameters β , Δ_{host} and σ_{int}

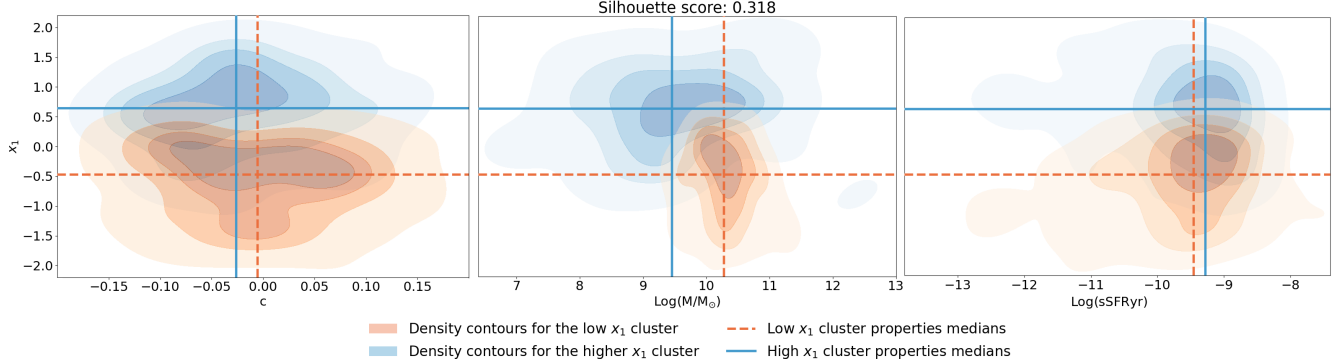


Fig. 14: Density contours of x_1 as a function of c (left), $\log(M/M_\odot)$ (middle), and $\log(\text{sSFRyr})$ (right) for the two identified clusters, representing the high-stretch (blue) and low-stretch (orange) SN subpopulations. Dashed lines indicate the median values of each property distribution for the low- x_1 cluster, while solid lines indicate the corresponding medians for the high- x_1 cluster. The median x_1 value for the low-stretch cluster is $\tilde{x}_1 = -0.475$ while for the high-stretch cluster it is $\tilde{x}_1 = 0.640$.

vious analysis presented in C.1 and discussed in Subsection 4.5, despite showing much less significant discrepancies. Several factors may account for this behavior.

First, when comparing our stretch distributions for each SN subpopulation with those reported in previous studies based on larger samples (e.g., Wojtak & Hjorth 2022; Ginolini et al. 2025; Wojtak, R. & Hjorth, J. 2025) who found nearly coinci-

Cluster	Number of SNe	H_0	Sig.	M_B	Sig.	α	Sig.
Low-stretch (orange)	108	$74.769^{+1.325}_{-1.318}$	1.19σ	$-19.185^{+0.036}_{-0.035}$	0.87σ	$0.143^{+0.022}_{-0.021}$	0.67σ
High-stretch (blue)	145	$72.473^{+1.399}_{-1.390}$		$-19.231^{+0.040}_{-0.042}$		$0.125^{+0.017}_{-0.018}$	

Table 15: Estimated H_0 , M_B and α using SNe each cluster obtained using the GMM clustering algorithm and their respective difference to the 16th and 84th percentiles. The right-hand columns report the significance of the differences between the estimated parameters for each bin of the considered property.

Cluster	Number of SNe	β	Sig.	Δ_{host}	Sig.	σ_{int}	Sig.
Low-stretch (orange)	108	$2.692^{+0.156}_{-0.153}$	1.13 σ	$-0.024^{+0.013}_{-0.013}$	0.12 σ	$0.102^{+0.014}_{-0.014}$	1.41 σ
High-stretch (blue)	145	$2.964^{+0.176}_{-0.182}$		$-0.026^{+0.011}_{-0.011}$		$0.074^{+0.014}_{-0.015}$	

Table 16: Same as Table 15 for the remaining parameters β , Δ_{host} and σ_{int}

dent Gaussian distributions describing the stretch populations, we find that while the higher-stretch distribution in our analysis closely agrees with the literature, the lower-stretch distribution exhibits substantially higher values than those previously reported, as we can see in Figure 15. Assuming that the x_1 distributions proposed in the literature are more closely representative of the expected behavior for each SN subpopulation, not only because of the consistency across multiple studies but also due to the larger sample sizes and methodology employed, our lower-stretch cluster is likely contaminated by SNe belonging to the higher-stretch population.

In addition, our Gaussian Mixture fitting relies solely on the x_1 and $\log(M/M_\odot)$ distributions. However, several other host-environmental properties, such as the local host colour, sSFR (e.g., Sullivan et al. 2010; Ginolini et al. 2025) and environment-based progenitor age (e.g., Nicolas et al. 2021), are also strongly correlated with stretch and could provide additional constraints on the underlying distributions of both SN subpopulations. The GMM clustering also have its own limitations. The algorithm is somewhat sensitive to outliers, as Gaussian mixture models assume that the features are normally distributed and assign all data points to the identified clusters. Moreover, contamination of the data by noise or outliers can further lead to misclassification of the underlying subpopulations (Kasa & Rajan 2023).

potential advantages and disadvantages. We also present the slopes obtained from linear regressions between the estimated parameters (H_0 , M_B , α , β , Δ_{host} and σ_{int}) and the different metrics used to evaluate the consistency between the calibration and Hubble Flow subsamples.

D.1. Sum and product of p -values

To evaluate the influence of the overall distribution concordance, we decided to plot the estimated parameters as a function of the logarithm of the sum and product of the p -values obtained when comparing each property distribution of the calibration and Hubble Flow subsamples using the one dimensional K-S Test, as shown in the left and right panels of Figure 16, respectively.

When generating random subsamples from the calibration and Hubble Flow, it is expected that some property distributions may closely match those of the calibration subsample, resulting in very high one-dimensional p -value, while others may not, resulting in very low p -value. This can lead to large discrepancies between the individual p -values estimated for different properties distributions within the same subsample. By using only the sum of all p -values, the higher p -values will dominate the result, overshadowing the contribution of the smaller values. This effect is evident in the left panel of Figure 16, which shows that the total sum of p -values increases with the difference between the highest and lowest p -values obtained for each subsample. This can give the misleading impression that most subsamples are consistent across all properties when $p_{sum} > 0.05$, while this apparent consistency is primarily driven by the highest p -value among the properties within each subsample

On the other hand, using the direct product of the one-dimensional p -values will cause extremely high or low values to dominate the result. As shown in the right panel of Figure 16, most subsamples have a low minimum p -value (mostly below 0.05). However, their p -value product is still higher than that of a subsample in which the distributions of c , x_1 , $\log(M/M_\odot)$, and $\log(\text{sSFR})$ in the calibration and Hubble flow subsamples all match, with all one-dimensional p -values above the 0.05 significance level. Despite having a higher p -value product, these subsamples are not in full concordance with each other, since at least one of their individual p -values falls below the significance threshold. While the product metric includes information from all parameters, its sensitivity to extremely higher or lower values limits its ability to assess whether both subsamples are in full agreement.

The slopes and corresponding uncertainties obtained from the linear regressions between the estimated parameters and the two metrics are presented in Table 17. These results are consistent with those shown in Figure 5 and discussed in Section 4.3.

D.2. Minimum p -value

We also defined the minimum p -value as the lowest among the four values obtained from the one-dimensional K-S tests comparing the distributions of the light curve parameters and host

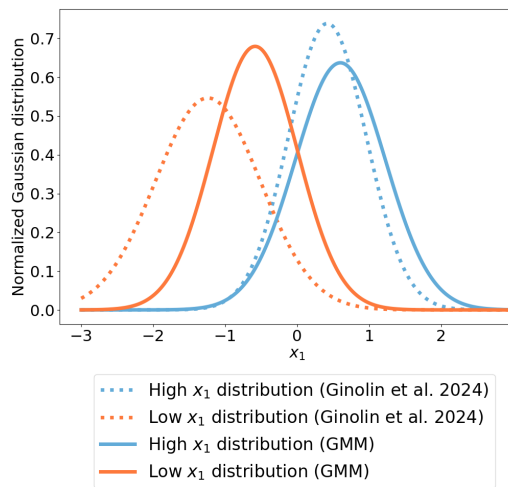


Fig. 15: Normalized Gaussian distributions representing the high-stretch (blue) and low-stretch (orange) SN populations, using the fitted parameters from Ginolini et al. (2025) (dotted lines) and the parameters estimated in this work using the GMM clustering algorithm (solid lines).

D. Using other matching metrics

In this chapter, we explore alternative metrics to the multi-dimensional K-S test used throughout this study, discussing their

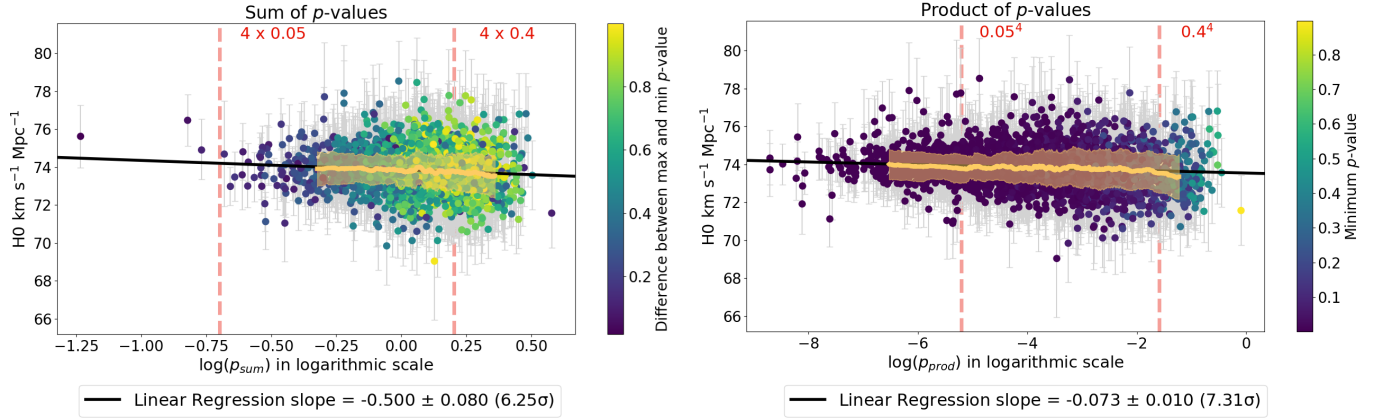


Fig. 16: Similar to analysis shown in the left panel of Figure 5 for H_0 when using the sum (left) or the product (right) of the individual p -values as the overall matching metric. The colormap in the left panel represents the difference between the highest and lowest p -values among the c , x_1 , $\log(M/M_\odot)$ and $\log(\text{sSFRyr})$ distributions estimated for each subsample, while the colormap in the right panel represents the lowest p -value of each subsample. The red dashed lines indicate the obtained metric values corresponding to a subsample where all p -values are 0.05 or 0.4.

Parameter	Sum of p -values (p_{sum})		Product of p -values (p_{prod})	
	Linear Regression Slope	Sig.	Linear Regression Slope	Sig
H_0	$(-4.995 \pm 0.800) \times 10^{-1}$	6.25σ	$(-7.288 \pm 0.997) \times 10^{-2}$	7.31σ
M_B	$(-1.845 \pm 0.190) \times 10^{-2}$	9.72σ	$(-2.857 \pm 0.236) \times 10^{-3}$	12.13σ
α	$(8.553 \pm 1.474) \times 10^{-3}$	5.80σ	$(1.272 \pm 0.184) \times 10^{-3}$	6.92σ
β	$(4.435 \pm 15.550) \times 10^{-3}$	0.29σ	$(1.932 \pm 1.942) \times 10^{-3}$	0.99σ
Δ_{host}	$(-2.335 \pm 1.150) \times 10^{-3}$	2.03σ	$(-3.704 \pm 1.436) \times 10^{-4}$	2.58σ
σ_{int}	$(-6.947 \pm 1.681) \times 10^{-3}$	4.13σ	$(-1.254 \pm 0.210) \times 10^{-3}$	5.99σ

Table 17: Slopes and uncertainties resulting from the linear regression between H_0 , M_B , α , β , Δ_{host} , and σ_{int} and either the sum (left column) or the product (right column) of the p -values obtained from comparing c , x_1 , $\log(M/M_\odot)$, and $\log(\text{sSFRyr})$ distributions between the calibration and HF samples using the one-dimensional K-S test, along with the corresponding significance levels.

properties between each calibration and HF subsample, providing a general metric to assess the overall concordance between their distributions. Indeed, we are expecting that increasing the minimum p -value should result in subsamples whose properties distributions match better and better as a higher minimum p -value necessarily implies that all individual p -values exceed that threshold, ensuring a level of concordance across all parameters. This allows us to use a single metric to evaluate the overall concordance across all properties distributions. However, a low minimum p -value may not necessarily indicate poor matching across all the considered distributions of c , x_1 , $\log(M/M_\odot)$, and $\log(\text{sSFRyr})$, as a subsample with a small minimum p -value could still exhibit high p -values for the remaining three properties, which gives some limitations on the use of the minimum p -value as a metric for overall distributional concordance.

As shown in the left panel of Figure 17, most subsamples have a minimum p -value below 0.05, which would suggest poor matching based on this metric. However, their median p -values are generally above 0.05, indicating that the low minimum p -value often reflects disagreement in just one property rather than across all properties. Nevertheless, the results obtained using this metric are consistent with the previous findings shown in left panel of Figure 5 and discussed in Section 4.3, as shown in Table presented in the right panel of Figure 17.

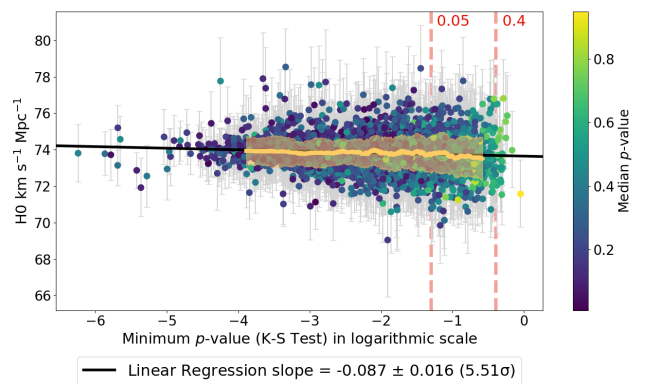


Fig. 17: Left panel: Similar to the analysis shown in the left panel of Figure 5 for H_0 when using the minimum p -values as the overall matching metric. The colormap represents the median p -value estimated from the c , x_1 , $\log(M/M_\odot)$ and $\log(\text{sSFRyr})$ distributions estimated for each subsample.

D.3. Energy distance based on the Wasserstein metric

The Wasserstein distance measures how different two probability distributions are by quantifying the minimum “work” required to transform one into the other, where work is defined as the amount of probability mass moved times the distance it is transported. This allows it to capture differences in both shape and location of the distributions (see Panaretos & Zemel 2019). The concept is rooted in optimal transport theory, introduced by Monge (1784), which seeks the least-cost mapping between two distributions. In the discrete case, the Wasserstein distance corresponds to the minimal total cost of an optimal transport plan that reallocates mass from one distribution to match the other. In this approach, we used the python implementation of this algorithm⁶ provided by the SciPy library (Virtanen et al. 2020) that allow us to compute the 1st Wasserstein distance between two N-dimensional discrete distributions.

The Energy Distance is a statistical measure used to quantify the dissimilarity between two probability distributions (see Rizzo & Székely 2016). It is based on the idea of comparing the expected pairwise distances between samples, capturing both the separation between the distributions, as well as their internal variability. In this method, we use the Wasserstein metric to estimate the expected pairwise distances between samples, contrary to the typically Euclidian distance. To estimate the Energy distance, we used the python implementation⁷ of the energy distance algorithm provided by the SciPy library (Virtanen et al. 2020).

To assess whether the differences measured by these distances are statistically significant, we apply a permutation test (Fisher 1935; Pitman 1937). This non-parametric test evaluates how likely it is that the observed difference between two samples could arise by chance. By repeatedly reshuffling the data labels and recalculating the distance-based statistic, we build a reference distribution that represents the null hypothesis that the two samples are drawn from the same population. The fraction of reshuffled datasets that produce a difference as large as the observed one yields the p -value, allowing us to determine whether the samples differ significantly without assuming any specific underlying distribution.

This method offers several advantages over previous approaches, including the multi-dimensional K-S test. In particular, the Wasserstein distance allows us to quantify the distance between all points in two different distributions. The Wasser-

stein distance evaluates the differences across the entire distribution, rather than only the maximum difference between cumulative distribution functions as the K-S test does. This provides a more complete measure of the difference between the samples and allows for better distinction between them. Furthermore, Ramirez et al. (2024) shows that optimal transport interpolation generates spectral time series that closely match the originals, with errors increasing more slowly than with linear interpolation. These findings suggest that the Wasserstein distance not only captures differences in the spatial displacement of distributions, but also preserves differences in their shapes with high accuracy. However, despite its potential advantages, this methodology is still under development, as computing the energy distance using the Wasserstein distance for multi-dimensional samples remains highly computationally demanding (see Panaretos & Zemel 2019). Since the multi-dimensional K-S test already provides a robust approach for comparing distributions and the metric discussed in this Section is not yet fully established, we chose not to adopt it as the primary comparison metric throughout this work. Nevertheless, we include in Table 19 the slopes obtained from linear regressions between the estimated parameters and the p -values computed when comparing the property distributions of the calibration and Hubble Flow samples using the energy distance with the Wasserstein metric. The permutation test used to calculate these p -values was based on 1000 permutations for each subsample.

Parameter	Energy distance p -value	
	Linear Regression Slope	Sig.
H_0	$(-0.059 \pm 0.015) \times 10^{-2}$	3.85σ
M_B	$(-3.418 \pm 0.360) \times 10^{-3}$	9.48σ
α	$(1.664 \pm 0.280) \times 10^{-3}$	5.95σ
β	$(3.468 \pm 2.950) \times 10^{-3}$	0.59σ
Δ_{host}	$(-4.419 \pm 2.181) \times 10^{-4}$	1.13σ
σ_{int}	$(-1.567 \pm 0.331) \times 10^{-3}$	4.73σ

Table 19: Slopes and uncertainties resulting from the linear regression between H_0 , M_B , α , β , Δ_{host} , and σ_{int} and the p_E obtained from comparing the calibration and HF samples using the Energy distance with the Wasserstein metric, along with the corresponding significance levels.

⁶ https://docs.scipy.org/doc/scipy/reference/generated/scipy.stats.wasserstein_distance_nd.html

⁷ https://docs.scipy.org/doc/scipy/reference/generated/scipy.stats.energy_distance.html